# JMST

Journal of Materials Science & Technology

ISSN 1005-0302

20 July 2025
Volume 224

材料科学技术（英文）


**COVER STORY**
**Chao Yang, Zhao Shen, Xiaoqin Zeng, et al.,**
**J. Mater. Sci. Technol. 224 (2025) 312-327.**

ELSEVIER

**Sponsored by**

Chinese Society for Metals | Chinese Materials Research Society | Institute of Metal Research, CAS

Journal of Materials Science & Technology 224 (2025) 312–327

Contents lists available at ScienceDirect

Journal of Materials Science & Technology

journal homepage: www.elsevier.com/locate/jmst

Research Article

# Simultaneous improvement of wear and corrosion resistance of microarc oxidation coatings on ZK61 Mg alloy by doping with $ZrO_2$ nanoparticles

Chao Yang[a], Chenyu Wang[a], Zhao Shen[a,b,*], Liping Zhou[a], Liyuan Sheng[c,d,**], Daokui Xu[e], Yufeng Zheng[c], Paul K. Chu[f], Shu Xiao[g,*], Tao Ying[a], Xiaoqin Zeng[a]

[a] National Engineering Research Center of Light Alloy Net Forming and State Key Laboratory of Metal Matrix Composites, School of Materials Science and Engineering, Shanghai Jiao Tong University, Shanghai 200240, China
[b] Institute of Medical Robotics, Shanghai Jiao Tong University, Shanghai 200240, China
[c] Shenzhen Institute, Peking University, Shenzhen 518057, China
[d] PKU-HKUST Shenzhen-Hong Kong Institution, Shenzhen 518057, China
[e] Key Laboratory of Nuclear Materials and Safety Assessment, Institute of Metal Research, Chinese Academy of Sciences, Shenyang 110016, China
[f] Department of Physics, Department of Materials Science & Engineering, and Department of Biomedical Engineering, City University of Hong Kong, Tat Chee Avenue, Kowloon, Hong Kong 999077, China
[g] School of Mechanical & Automotive Engineering, South China University of Technology, Guangzhou 510641, China

ARTICLE INFO

*Article history:*
Received 18 September 2024
Revised 22 October 2024
Accepted 25 October 2024
Available online 15 November 2024

*Keywords:*
ZK61 Mg alloy
Micro arc oxidation
$ZrO_2$ doping
$MgF_2$
Wear resistance
Corrosion resistance

ABSTRACT

The poor corrosion resistance of magnesium (Mg) and its alloys limits their application in various fields. Micro arc oxidation (MAO) coatings can improve the corrosion resistance, but the pore defects and low surface hardness make them susceptible to wear and accelerated corrosion during usage. In this study, a $ZrO_2$ nanoparticles doped-MAO coating is prepared on the ZK61 Mg alloy by utilizing an $MgF_2$ passivation layer to prevent ablation. The $ZrO_2$ nanoparticles re-melt and precipitate due to local discharging, which produces evenly dispersed nanocrystals in the MAO coating. As a result, the hardness of the MAO coating with the appropriate $ZrO_2$ concentration increases by over 10 times, while the wear rate decreases and corrosion resistance increases. With increasing $ZrO_2$ concentrations, the corrosion potentials increase from −1.528 V of the bare ZK61 Mg alloy to −1.184 V, the corrosion current density decreases from $1.065 \times 10^{-4}$ A $cm^{-2}$ to $3.960 \times 10^{-8}$ A $cm^{-2}$, and the charge transfer resistance increases from $3.41 \times 10^2$ Ω $cm^2$ to $6.782 \times 10^5$ Ω $cm^2$. Immersion tests conducted in a salt solution for 28 d reveal minimal corrosion in contrast to severe corrosion on the untreated ZK61 Mg alloy. $ZrO_2$ nanoparticles improve the corrosion resistance of MAO coatings by sealing pores and secondary strengthening of the corrosion product layer.



## 1. Introduction

Magnesium (Mg) has a density of about 2/3 of that of aluminum and 1/4 of that of steel. In addition, it has advantages such as high strength, good vibration damping, and biocompatibility making it and its alloys promising materials for aerospace applications, automobiles, and implantable medical devices [1–5]. However, since Mg has a negative standard electrode potential (−2.37 V), micro-galvanic corrosion occurs when there is a high-potential second phase in the Mg alloy [6–8]. Although processing like heat treatment or extrusion can reduce micro-galvanic corrosion, the porous $Mg(OH)_2$ corrosion product film has poor long-term corrosion resistance, especially in a corrosive medium [9,10].

Surface treatment such as deposition of chemical conversion films, chemical plating, micro-arc oxidation (MAO), and anodization [11–13] can improve the surface properties of Mg alloys. For example, MAO produces a surface ceramic layer to increase the corrosion resistance [14–16]. However, because of electrical discharges during MAO, the surface is typically porous thus allowing penetration of the corrosive medium and local corrosion of the substrate during long-term service [17,18]. Hence, organic sealing, layered double hydroxides (LDH) and surface hydrophobic treat-

* Corresponding author.
** Corresponding author at: PKU-HKUST Shenzhen-Hong Kong Institution, Shenzhen 518057, China.
*E-mail addresses:* shenzhao081@sjtu.edu.cn (Z. Shen), lysheng@yeah.net (L. Sheng), xiaos@scut.edu.cn (S. Xiao).

https://doi.org/10.1016/j.jmst.2024.10.023
1005-0302/

ment have been proposed to improve the corrosion resistance [19–23]. However, organic materials are prone to aging leading to sealing failure [24], LDH and the hydrophobic surface structure has poor mechanical stability [25–27]. By doping with corrosion-resistant nanoparticles of ZnO, $CeO_2$, and $TiO_2$ or compounds such as calcium phosphate and zinc phosphate, the porous channels can be blocked to enable self-healing [28–30]. However, the main phase of MAO coatings on Mg alloys is usually MgO, which has low hardness and cannot meet the wear requirements for many applications [31,32]. Moreover, worn MAO coatings cannot protect the substrate adequately [33,34]. Therefore, for industrial applications, it is important to improve both the wear and corrosion resistance of MAO coatings.

Generally, the use of aluminate electrolytes, mainly $NaAlO_2$, can result in the formation of a highly wear resistant $MgAl_2O_4$ spinel phase (~16 GPa) within MAO coatings [35,36]. However, compared to phosphate or silicate electrolytes, the MAO coatings prepared by aluminate electrolytes exhibit poorer corrosion resistance [37]. To address this issue, researchers used a dual electrolyte containing phosphate and aluminate to perform MAO on Mg alloys, achieving a synergistic improvement in corrosion resistance and wear resistance of the coating [38,39]. However, the competitive oxidation mechanism of dual electrolytes remains unclear, and pore defects cannot be completely avoided. In recent years, the rapid development of two-dimensional materials, such as GO and $MoS_2$, has provided an effective avenue for the advancement of high-performance devices [40,41]. By modifying them and doping with MAO, the wear resistance and corrosion resistance of the coating have been significantly improved [42,43]. This can be attributed to the self-lubrication of the two-dimensional materials and the reduced electron transfer ability after modification [44]. However, the high cost and unstable doping process associated with these materials pose significant challenges to their commercialization. Therefore, exploring new alternative materials or new enhancement strategies has become crucial.

$ZrO_2$ nanoparticles are used as a stiff phase in MAO coatings to improve the hardness [45,46] and incorporation of a trace amount of Zr into Mg alloys enables densification of the corrosion product film [10,47,48]. During corrosion, Zr is oxidized to form $ZrO_2$, which can fill the pores in the $Mg(OH)_2$ corrosion product and densify the corrosion product film [10,49]. In general, nanoparticles are partially melted during doping to assist in coating growth. After cooling, they precipitate as nanocrystals, enhancing the intrinsic functionality of the coating. Un-melted particles aggregate due to the electric field, playing a sealing role in the process [29,30]. However, when the concentration of $ZrO_2$ nanoparticles is high, the MAO coating is prone to ablation thus affecting the stable growth of the coating and rapidly reduces its corrosion resistance [50]. In view of this, by adjusting the current to control the anode-cathode charge ratio (RCQ) to be between 0.8 and 1 or reducing the power in the later stage of coating growth to form "soft spark" discharge, ablation can be delayed [51,52]. However, a smaller power decreases the coating thickness and dopant concentration [53].

Generally, the discharge of MAO coating is that the surface passivation layer breaks down at a certain voltage, and the difficulty of breakdown is related to the dielectric constant. Therefore, using a passivation layer with a low dielectric constant can effectively alleviate the voltage without reducing the number of arcs [29]. This passivation layer design provides a strategy to enhance the doping of high content functional phase $ZrO_2$ nanoparticles in MAO coatings. In this study, a $MgF_2$ passivation layer with low dielectric constant is prepared using an electrolyte containing F, and a MAO coating doped with high content $ZrO_2$ nanoparticles is fabricated on ZK61 Mg alloy. The phases and composition of the MAO coating are determined. In addition, the mechanical properties such as hardness and friction as well as corrosion resistance are assessed systematically. Based on the electrochemical and immersion tests as well as corrosion products, the corrosion mechanism is studied and described.

## 2. Experimental

### 2.1. Materials

The ZK61 Mg alloy (30 mm × 30 mm × 1 mm) was purchased from Suzhou Chuanmao Metal Materials Co., Ltd. (China) and its elemental composition is listed in Table S1 in the Supporting information. The chemical reagents such as acetone, anhydrous ethanol, sodium hydroxide, sodium chloride, sodium hexametaphosphate, and sodium fluoride were analytical grade and bought from Sinopharm Chemical Reagent Co., Ltd. (China). The $ZrO_2$ nanoparticles were supplied by Aladdin Biochemical Technology Co., Ltd. (China). All the reagents were used as received without further purification.

### 2.2. Preparation of MAO coatings

The ZK61 Mg alloy was polished with sandpaper (2000 grit) and cleaned with deionized water, ethanol, and acetone for 30 min each. The MAO electrolyte was prepared by mixing 15 g $L^{-1}$ sodium hexametaphosphate, 5 g $L^{-1}$ sodium hydroxide, and 3 g $L^{-1}$ sodium fluoride. Among them, due to the sodium fluoride have positive effect on the corrosion resistance of coating, so it was chosen as an anionic additive [54]. A 15 kW AC power supply was used in the MAO apparatus with the Mg alloy sample as the anode and the stainless steel container as the cathode. Discharge experiments were conducted in the constant current mode at a current density of 5 A $dm^{-2}$, frequency of 200 Hz, and duty cycle of 15 %. The electrolyte temperature was maintained below 45 °C. The coatings doped with 0, 3, 6, and 9 g $L^{-1}$ $ZrO_2$ nanoparticles were labeled as MAO, Zr-3, Zr-6, and Zr-9, respectively. When the concentration continues to increase, it will cause a rapid rise in voltage, and the control of the passivation layer cannot alleviate the ablation behavior. Therefore, the highest doping content here is determined to be 9 g $L^{-1}$.

### 2.3. Characterization

A field-emission scanning electron microscope (FE-SEM, Carl Zeiss, SUPRA® 55, GER) was employed to observe the microstructure of the $ZrO_2$ nanoparticles and MAO coatings, and energy-dispersive X-ray spectroscopy (EDS, GB) was used for elemental analysis. The surface elemental content of all samples before and after corrosion was quantitatively analyzed by EDS. X-ray diffraction (XRD, Bruker, D8 Advance, GER) was carried out at a $2\theta$ range of 10°~80° The cross-sections with a thickness of <100 nm were obtained by a focused ion beam (FIB, Scios, FEI, USA) prior to high-resolution transmission electron microscopy (TEM, JEM-3200FS, Japan). To assess the worn and corroded pits, a 3D laser confocal scanning microscope (LCSM, VK-X200 series, USA) was utilized. The coating thickness and surface roughness were determined from the SEM and LCSM images.

### 2.4. Tribological tests

A friction and wear tester (Rtec, MFT-5000, USA) was employed in the friction and wear experiments at room temperature. A $Si_3N_4$ ball with a diameter of 4 mm was the counter specimen in the test with a rotation diameter of 5 mm and rotation speed of 100 r $min^{-1}$. The tribological properties were determined after the 10-min friction test at a load of 3 N load in order to evaluate the

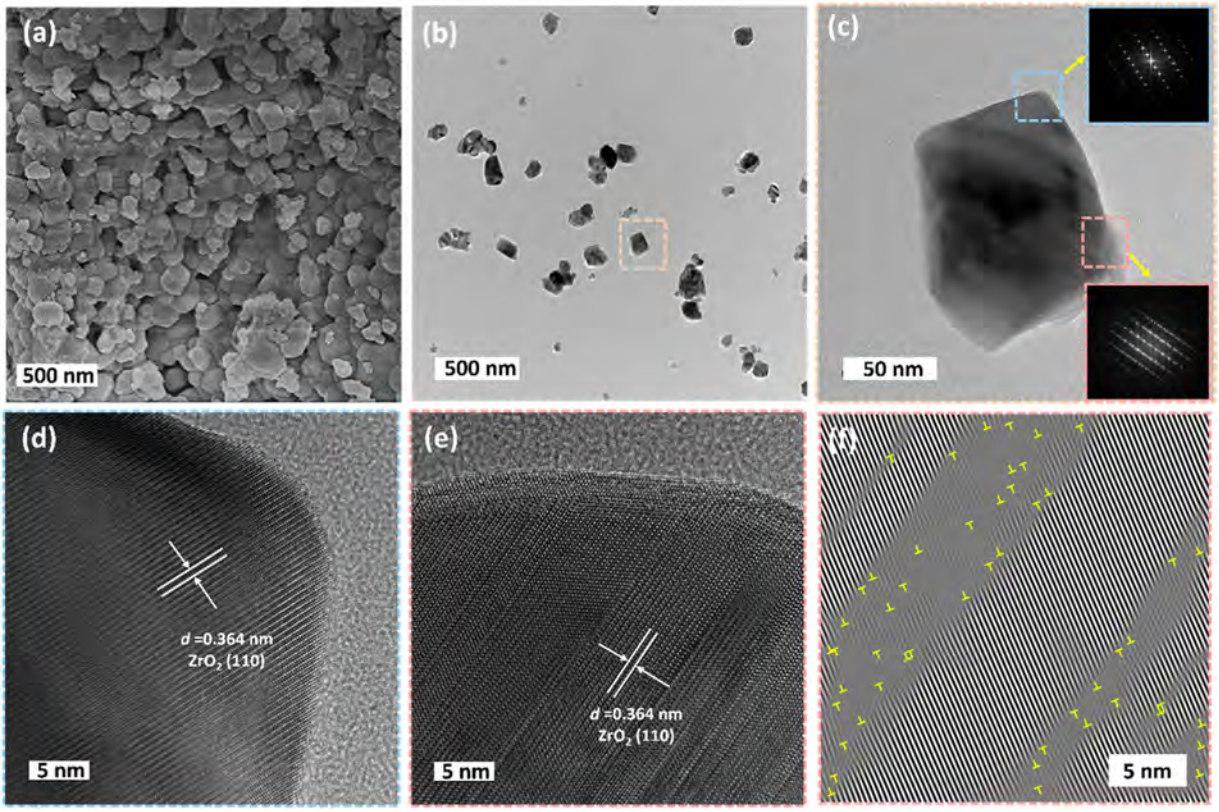


**Fig. 1.** Morphology and crystal structure of the $ZrO_2$ nanoparticles: (a) SEM image showing the polyhedral structure of $ZrO_2$ nanoparticles, (b) TEM image showing $ZrO_2$ nanoparticles with a nearly rectangular shape, (c) TEM image of a $ZrO_2$ nanoparticle showing the face-centered cubic structure (Inset images showing the SAED patterns of the corresponding regions), (d) HR-TEM image showing the perfect crystal structure, (e) HR-TEM image showing micro-twins and stacking faults, and (f) IFFT image of Fig. 1(e) showing the dislocations along the boundaries of stacking faults.

tribological properties of the materials. The wear rate $W$ ($mm^3$ $N^{-1}$ $m^{-1}$) was determined by the following equation:

$$W = V/(F \times t \times 2\,pnr) \quad (1)$$

where $V$ ($mm^3$) is the wear volume, $F$ (N) is the applied load, $t$ (s) is the wear time, $n$ (m $s^{-1}$) is the rotation speed, and $r$ (m) represents the rotating radius. Five measurements were made to generate the average wear rates.

### 2.5. Corrosion resistance evaluation

The corrosion resistance was assessed by electrochemical tests and immersion experiments. The electrochemical workstation (chi660e, China) consisted of a three-electrode cell in the 3.5 wt% NaCl solution at room temperature. The working electrode of the Mg alloy sample with a 1 $cm^2$ of exposed area, while the reference and counter electrodes were the saturated calomel electrode (SCE) and Pt. To stabilize the system, the open circuit potential (OCP) test was conducted in the 3.5 wt% NaCl solution for 10 min. Electrochemical impedance spectroscopy (EIS) was determined using a sinusoidal signal with an amplitude of 10 mV in the frequency range of 100 kHz to 0.1 Hz. The impedance data were fitted and analyzed by the ZsimpWin software (USA). The Tafel data were obtained at a scanning rate of 1 mV $s^{-1}$. The corrosion potentials and corrosion current densities were calculated by extrapolation. The corrosion potential is the intersection potential of the cathode and the anode branches, while the corrosion current density represents the intersection current density of the anode curve and the cathode curve at the tangent line. In the immersion experiments, the samples were immersed in the 3.5 wt% NaCl solution at room temperature in 100 mL beakers for five different time durations (1, 3, 7, 14, and 28 d) and examined by LCSM. After the immersion test, the samples were cleaned and the corrosion products were analyzed.

## 3. Results and discussion

### 3.1. Microstructure and phase

The morphology and crystal structure of the $ZrO_2$ nanoparticles are exhibited in Fig. 1. The nanoparticles are mostly polyhedrons with an average size of about 100 nm (Fig. 1(a)) and most of them have a nearly rectangular structure (Fig. 1(b)). The crystal defects are visible in Fig. 1(c). Selected-area electron diffraction (SAED) reveals a perfect crystal structure in some areas, but the other regions show micro-twinning and stacking faults indicative of inner stress. The HR-TEM images are depicted in Fig. 1(d, e). The $ZrO_2$ nanoparticles prefer to grow along the (110) plane and the spacing is 0.364 nm in agreement with face-centered cubic zirconia crystal [55]. HR-TEM shows the existence of interfaces in the crystal and combined with the SAED pattern, micro-twins and stacking faults are inferred. Inverse fast Fourier transformation (IFFT) indicates that many dislocations form along the boundaries of the stacking faults, as shown in Fig. 1(f).

Fig. 2 shows the variation of the discharge potentials-time in MAO process and corresponding schematic diagrams. Even when the $MgF_2$ passivation layer is regulated, the addition of $ZrO_2$ nanoparticles to the electrolyte affects the discharge potentials. The discharge curve can be divided into three stages: the formation stage of the surface passivation layer (0–30 s), the arc discharge stage (30–420 s), and the growth stage (420–600 s). In phosphate electrolytes, the ZK61 magnesium alloy first undergoes oxidation, forming a MgO passivation layer. When the electrolyte is doped

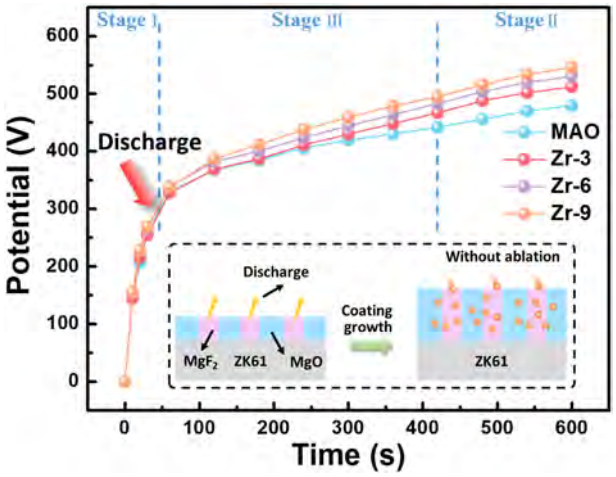


**Fig. 2.** Discharge curves during MAO of the ZK61 Mg alloy in electrolyte with $ZrO_2$ nanoparticles with the regulation of the $MgF_2$ passivation layer (Inset showing the role of the passivation layer in regulating the coating growth).

with F salt, a passivation layer structure composed of $MgF_2$ and MgO is formed [29]. Due to the lower dielectric constant ($\varepsilon$ = 5.45 F $m^{-1}$) of $MgF_2$ compared to MgO ($\varepsilon$ = 9.65 F $m^{-1}$) [56], electron avalanche can first occur along $MgF_2$ at an appropriate low voltage, while electron avalanche does not occur in adjacent MgO. In this case, after $MgF_2$ electric melting heating, adjacent MgO begins to discharge under the action of the electric thermal coupling field. Therefore, the discharge first occurs in the area where $MgF_2$ accumulates, leading to arc discharge. The voltage-time curve of the passivation layer growth stage (0–30 s) indicates that the voltage increases with $ZrO_2$ nanoparticles. This is because the $ZrO_2$ nanoparticles do not yet participate in the growth process of the passivation layer and F is more likely to form insulating compounds with Mg compared to O, resulting in a faster voltage increase.

In the arc discharge stage (30–420 s), the voltage increases gradually and is higher for a larger concentration of $ZrO_2$ nanoparticles due to the thickening of the insulating passivation layer and charge buildup on the surface resembling a capacitor. Consequently, the voltage increases gradually until the breakdown voltage of $MgF_2$ which has a low dielectric constant. In this stage, an arc is formed as it breaks through the passivation layer to create discharge channels for $ZrO_2$ nanoparticles. However, the conductivity of $ZrO_2$ nanoparticles is poor, resulting in greater resistance and more significant voltage increases at higher doping concentrations. After 420 s, the discharge enters the stage of coating growth. The coating thickens rapidly causing the discharge voltage to increase and the arc discharge to intensify. In typical MAO coatings, when a certain voltage threshold is reached, the coating is repeatedly broken down at relatively weak positions leading to local ablation. The larger the concentration of $ZrO_2$ nanoparticles, the faster the voltage increase and the more severe the ablation. Owing to the $MgF_2$ structure with a low dielectric constant, the MAO coating exhibits a lower breakdown voltage, which is beneficial to coating growth and delay of ablation.

The surface morphology of the MAO coatings prepared in electrolytes with different concentrations of $ZrO_2$ nanoparticles is examined by SEM and shown in Fig. 3. It has a porous structure

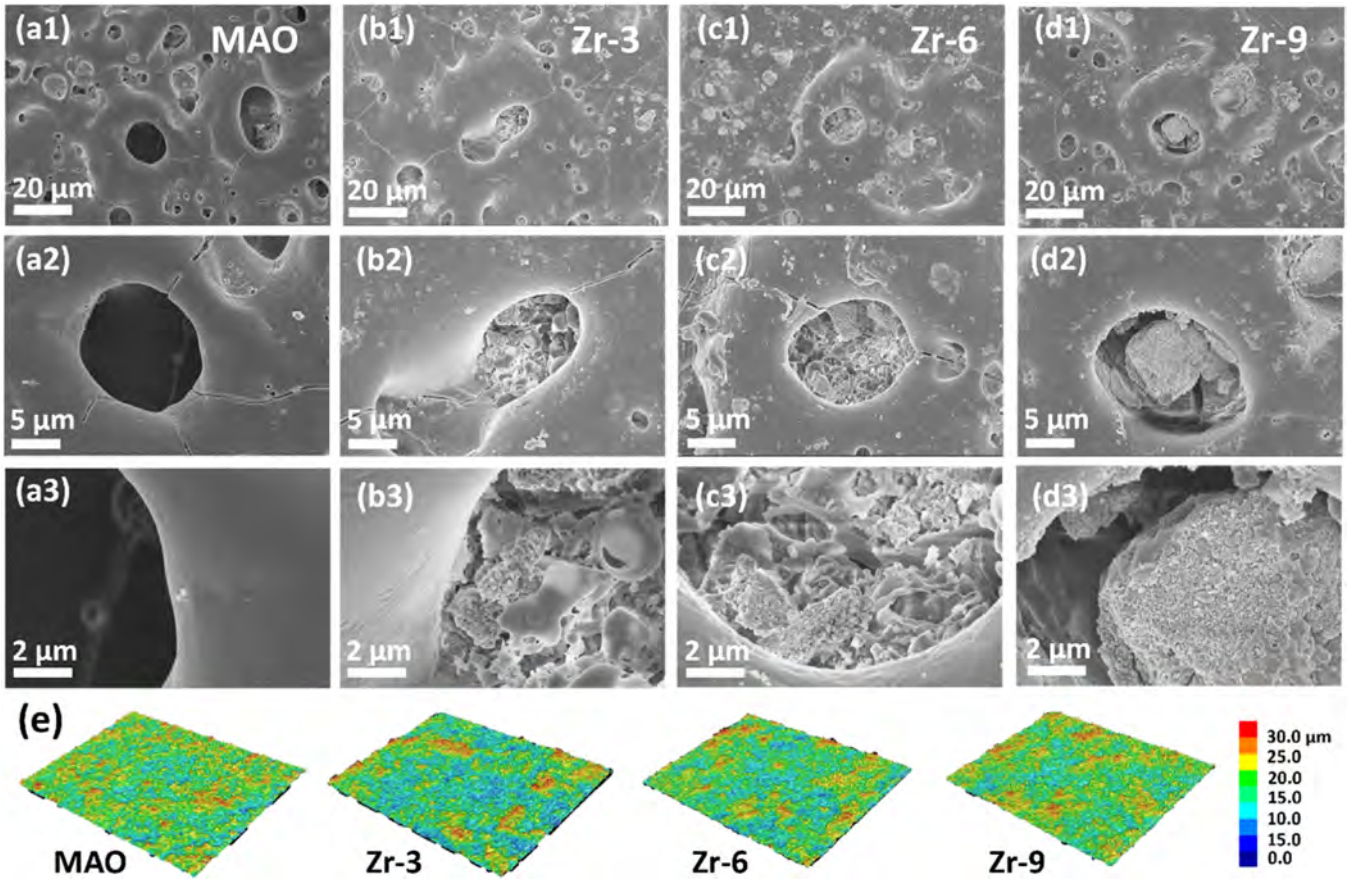


**Fig. 3.** SEM images of the MAO coatings doped with different concentrations of $ZrO_2$ nanoparticle: (a) MAO, (b) Zr-3, (c) Zr-6, and (d) Zr-9; (e) LCSM observations of different samples.

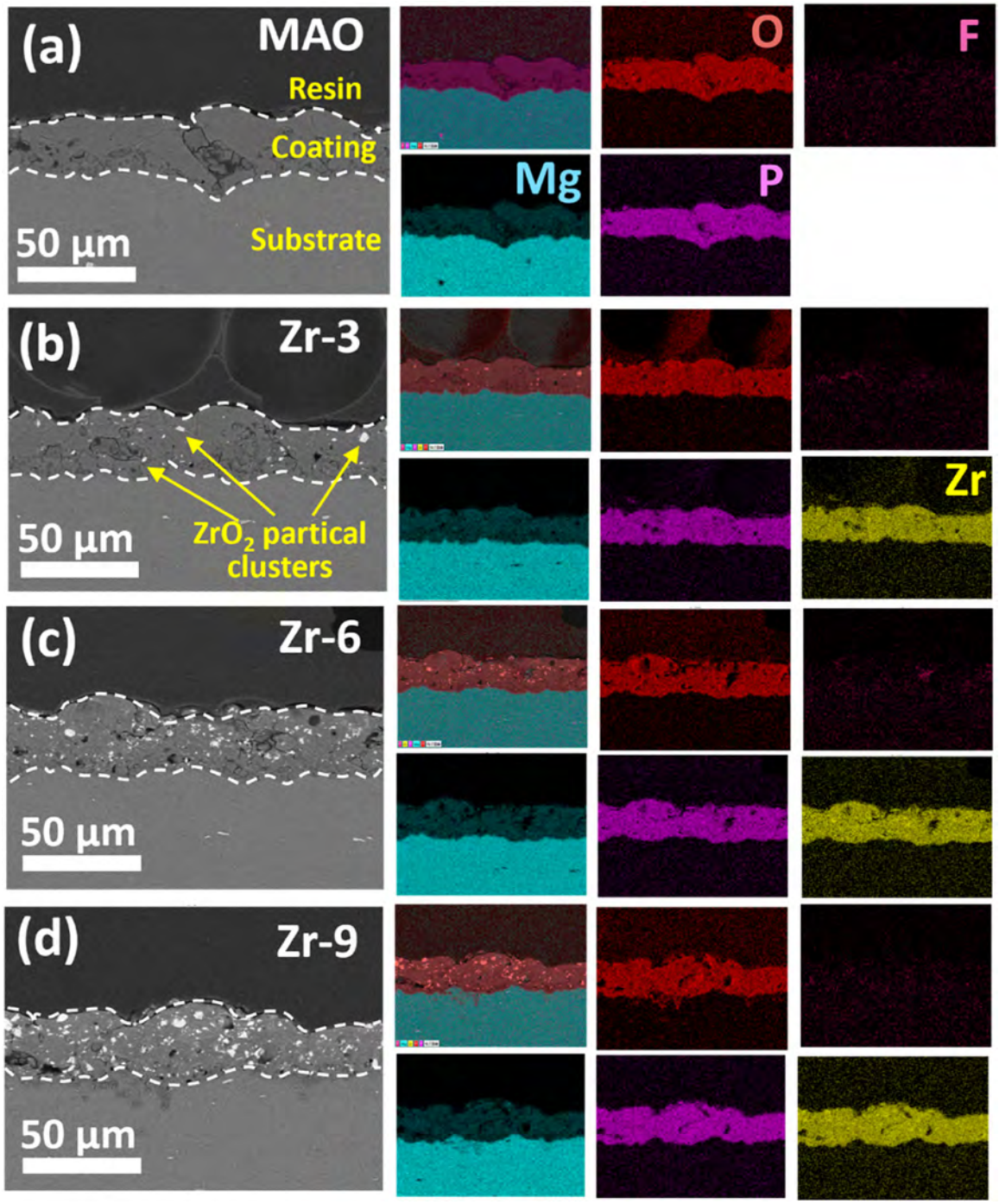


**Fig. 4.** Cross-sectional SEM images and EDS mapping of elemental distributions of the MAO coatings: (a) MAO, (b) Zr-3, (c) Zr-6, and (d) Zr-9.

resembling a volcanic crater with pore sizes range of 5–20 $\mu$m, as shown in Fig. 3(a1–a3). These features are formed because the local discharge generates a high-temperature and high-pressure microenvironment in the channels giving rise to the ejection of molten Mg from the discharge channels. The molten Mg reacts with the electrolyte and cools to form an oxide coating. Compared with the MAO sample, the pores in Zr-3, which is doped with a small amount of $ZrO_2$ nanoparticles, are partially filled with nanoparticle clusters and molten materials, as shown in Fig. 3(b1–b3). As the concentration of $ZrO_2$ nanoparticles increases, more nanoparticles gather inside the pores, leading to improved sealing effects, as shown in Fig. 3(c1–c3 and d1–d3). EDS confirms $ZrO_2$ aggregation inside the pores (Fig. S1) and LCSM reveals a rugged surface as shown in Fig. 3(e). However, the difference in surface roughness is not significant (Table S2).

Fig. 4 displays the cross-sectional morphology and elemental distributions of the MAO coatings doped with $ZrO_2$ nanoparticles. The thicknesses of coating do not change appreciably with $ZrO_2$ concentration. The thicknesses of MAO, Zr-3, Zr-6, and Zr-9 are 24.5 ± 2.6, 25.5 ± 1.8, 25.1 ± 2.1, and 24.9 ± 2.2 $\mu$m, respectively (Table S2), indicating that the growth rates are not affected by lower voltages. Moreover, the $MgF_2$ phase allows uniform growth even at lower voltages. $ZrO_2$ particle aggregates are observed from Zr-3, Zr-6, and Zr-9 and EDS shows that these aggregates are doped

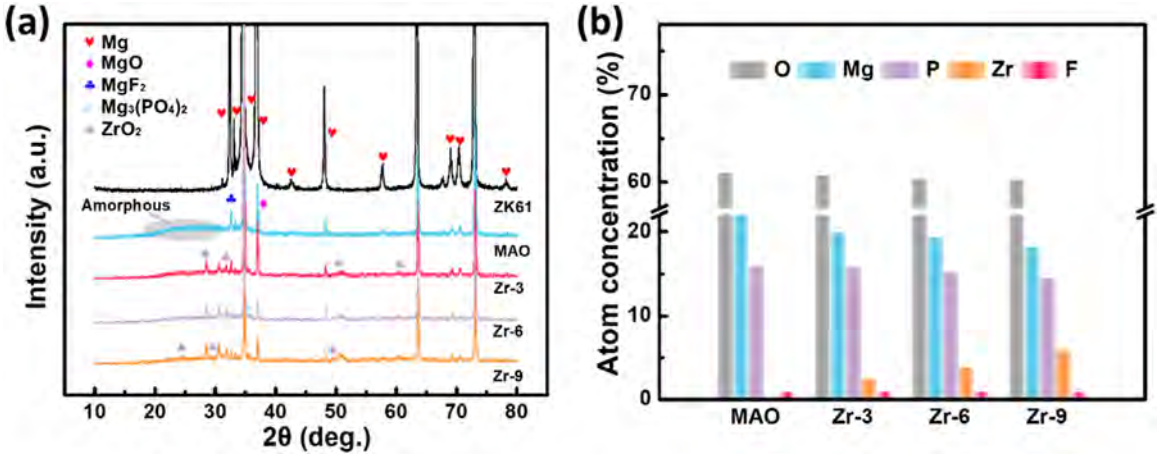


**Fig. 5.** Phase constituents and chemical composition of the MAO coatings doped with different concentrations of $ZrO_2$ nanoparticles: (a) XRD patterns and (b) surface elemental concentrations.

$ZrO_2$ nanoparticle clusters. Apart from the MAO sample, the coatings consist of primarily uniformly distributed Mg, O, F, P, and Zr.

Fig. 5(a) shows the XRD patterns of the MAO coatings prepared with different concentrations of $ZrO_2$ nanoparticles. The peaks between 30° and 75° are attributed to the Mg substrate (PDF-#35–0821). Peaks corresponding to $MgF_2$ (111) (PDF#38-0882) and MgO (111) (PDF-#45-0946) are observed at 32.3° and 36.9°, respectively, while the peak at 35.2° represents the (002) crystallographic plane of $Mg_3(PO_4)_2$ (PDF-#33–0876). Diffraction peaks associated with the crystal plane orientations of $ZrO_2$, such as (110), (011), ($\bar{1}$11), (111), (220), (022), and (121), appear at 24.0°, 30.3°, 31.5°, 48.9°, 49.3°, and 60.2° (PDF-#37-1484 and PDF-#50-1089). The intensity of $ZrO_2$ peaks increases gradually with $ZrO_2$ concentration and the largest intensity is observed from Zr-9. A broad peak representing the amorphous phase is observed between 20° and 30°. Additionally, the MAO coating doped with Zr also exhibits some peaks with lower intensity. This may be attributed to the formation of magnesium zirconium spinel, as MgO tends to bind to the external $ZrO_2$ interface during the remelting and peeling process of the MAO coating synthesis. Fig. 5(b) and Table S3 show the elemental contents of MAO coatings doped with different concentrations of $ZrO_2$ nanoparticles. The coating mainly comprises Mg, O, F, P, and Zr. The P concentration is approximately 15 at.% and the Zr concentration increases from 2.48 at.% in Zr-3 to 5.83 at.% in Zr-9 sample.

The cross-sectional TEM image of the of Zr-9 after thinning to 100 nm by FIB is displayed in Fig. 6. The EDS again reveals uniform distributions of Mg, O, F, and P elements, while Zr is concentrated on the surface, consistent with the SEM results, as shown in Fig. 6(a). Some regions have a high concentration of Zr, indicating aggregation of $ZrO_2$. Three selected locations are analyzed and there is distinct contrast as shown in Fig. 6(b). The TEM image of the highest contrast region reveals the presence of $ZrO_2$ nanoparticle clusters with a size of about 100 nm, as shown in Fig. 6(c). This is due to the partial aggregation of negatively charged $ZrO_2$ particles in the discharge channels. $ZrO_2$ particles with crystal defects can be observed from Fig. 6(d, f) disclose that the particle is surrounded by an amorphous layer. The interior of the $ZrO_2$ particle mainly grows along the (110) crystal plane, which is the same preferred orientation as the doped particles. The edge of the $ZrO_2$ particle has a special layer of $ZrO_2$ (111) with a thickness of 3 nm, indicating the potential influence of high temperature and pressure in the discharge channels. The extreme conditions transform of the $ZrO_2$ nanoparticle surface into lower energy (111) crystal planes. The SAED pattern confirms the presence of $ZrO_2$ (111) and (110) together with the amorphous, $Mg_3(PO_4)_2$ (002), and $MgF_2$ (111) phases, as shown in Fig. 6(g).

The TEM image acquired from another region reveals ultrafine precipitates, as shown in Fig. 6(e). Two random regions are examined by HR-TEM and exhibit different crystal structures. As shown in Fig. 6(h), the particles prefer to precipitate in twins. The $ZrO_2$ particle, with the (111) preferred crystallographic plane and a size of approximately 20 nm, coexists with the $MgF_2$ particle in the (111) preferred crystallographic plane, with a size of about 10 nm, embedded in the amorphous phase [57,58]. The $ZrO_2$ nanocrystals with different preferred crystallographic planes indicate remelting and precipitation of $ZrO_2$ nanoparticles during MAO. There are numerous nanoparticles with a size of about 10 nm with a random distribution, as shown in Fig. 6(i). The corresponding SAED patterns reveal that this region predominantly consists of MgO (111), $Mg_3(PO_4)_2$ (002), $MgF_2$ (111), $ZrO_2$ (111), $ZrO_2$ (110), and the amorphous phase. These findings suggest that the doped $ZrO_2$ in the MAO coating partly exists in the form of original particles or particle clusters with a smaller proportion, while the majority is uniformly dispersed ultrafine particles formed by re-melting and precipitation. This result is consistent with the performance of most nanoparticles doped in MAO coatings. This is because some nanoparticles partially melt at high temperatures in the discharge channel region (pores), enter the coating during growth, and precipitate in the form of nanocrystals when the coating cools. This process can alter the basic functional characteristics of the coating, such as corrosion resistance, hardness, and friction coefficient, etc [28–30]. Additionally, the un-melted nanoparticles in the discharge channel region (pores) aggregate due to the electric field, acting as a sealing agent, thereby improving corrosion resistance. The designed $MgF_2$ passivation layer significantly increases the doping content of $ZrO_2$ nanoparticles (Figs. 4 and 5) in order to improve the intrinsic properties of the coating and reduce the defects of weak pores.

### 3.2. Microhardness and tribological properties

As shown in Fig. 7(a), the hardness of ZK61 Mg alloy is 78 HV, while that of the MAO coating increases to 318 HV due to the *in situ* formed $MgO/MgF_2/Mg_3(PO_4)_2$ in the coating. With increasing $ZrO_2$ concentration, the hardness gradually increases due to the super-hardness (1200–1400 HV) of $ZrO_2$ in conjunction with the nano-size and uniform distribution. The hardness values of Zr-3, Zr-6, and Zr-9 are 689, 796, and 924 HV, respectively. The dispersion-strengthening effects of the $ZrO_2$ nanoparticles restrict

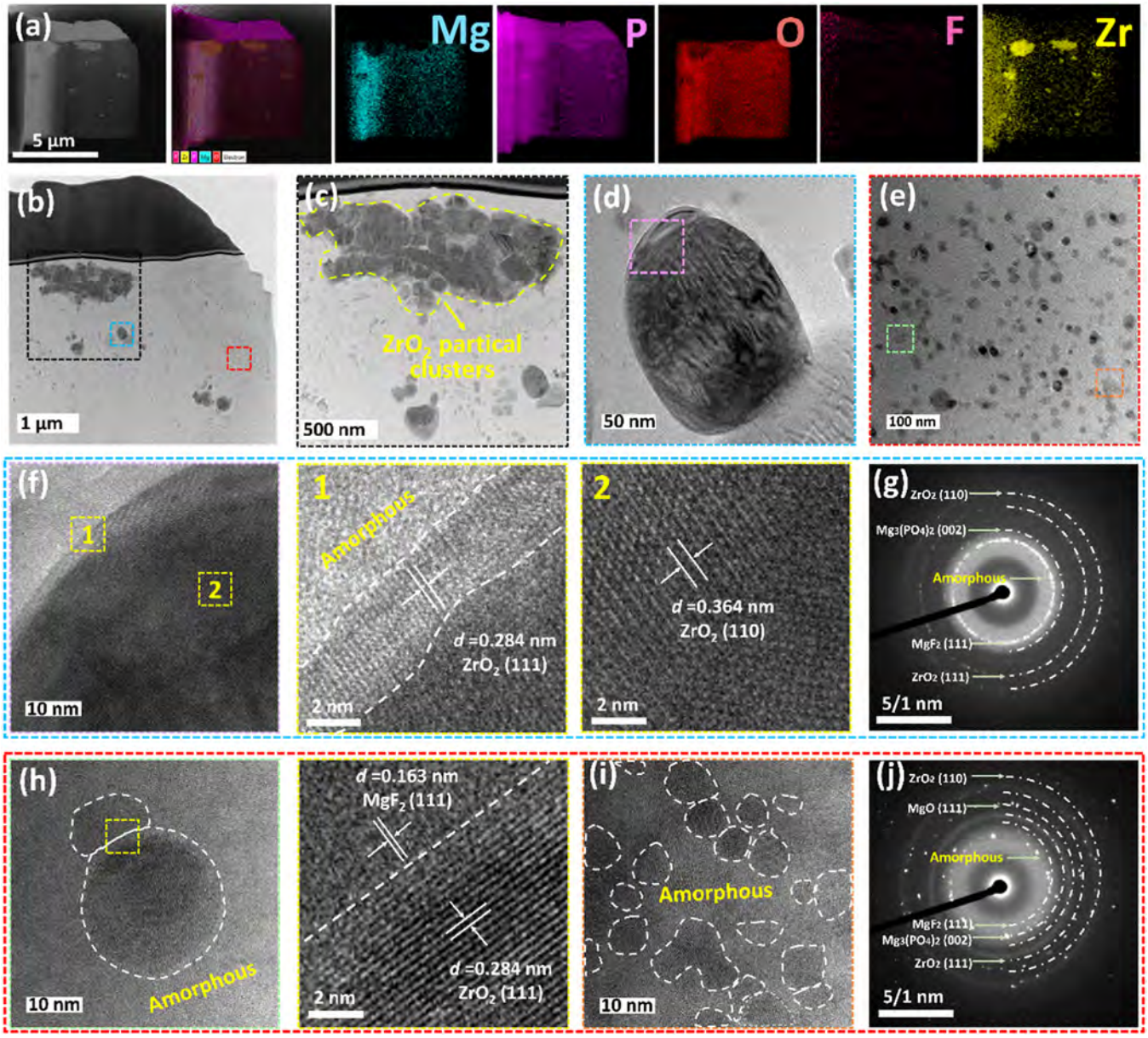


**Fig. 6.** TEM images of the cross-section of the Zr-9 coating: (a) EDS elemental maps; (b) low-magnification TEM image of three regions: (c) aggregated particles, (d) individual particles, and (e) precipitated nanocrystals; (f, g) HR-TEM image and SAED pattern of the individual particles; (h–j) HR-TEM image and SAED pattern of the precipitated nanocrystals.

the deformation of the MAO coating to improve the tribological properties. Friction experiments are conducted under a load of 3 N, as shown in the inset in Fig. 7(b, c). The friction coefficients of the ZK61 Mg alloy increase rapidly to about 0.35 within 40 s and fluctuate between 0.29 and 0.4 during the subsequent friction process. After deposition of the MAO coating, the friction coefficients increase to about 0.36 within 50 s and then go up gradually, reaching the maximum of 0.5 with a fluctuation of about 0.1. Comparatively, the friction coefficients of Zr-3 increase initially to about 0.4 within 30 s and then slightly decrease and increase again to about 0.5 in 80 s. Afterward, the friction coefficients decrease to 0.3 at about 300 s but with a fluctuation of 0.55 toward the end. The variation may be attributed to the relatively low doping concentration of $ZrO_2$. The porous morphology and aggregated $ZrO_2$ nanoparticles result in high initial friction coefficients, while the lack of stiffness in the phase leads to noticeable fluctuations in the friction coefficients, with both decreases and increases observed. The friction coefficients of Zr-6 and Zr-9 exhibit a similar trend with a rapid increase to about 0.4 and subsequent gradual increase to 0.55 at the end with fluctuation. Hence, the concentration of $ZrO_2$ nanoparticles and distribution could play an important role in the tribological properties of the MAO coating.

The wear rates of different samples after 600 s of friction test are given in Fig. 7(c). The ZK61 Mg alloy exhibits the highest wear rate of $2.68 \times 10^{-4}$ $mm^3$ $N^{-1}$ $m^{-1}$. However, the wear rate decreases to $7.50 \times 10^{-5}$ $mm^3$ $N^{-1}$ $m^{-1}$ after MAO, and by introducing $ZrO_2$ nanoparticles, the wear rates decrease further. The wear rates of Zr-3, Zr-6, and Zr-9 are $3.76 \times 10^{-5}$, $2.81 \times 10^{-5}$, and $1.84 \times 10^{-5}$ $mm^3$ $N^{-1}$ $m^{-1}$, respectively. MAO coating and doping with $ZrO_2$ nanoparticles enhance the wear resistance of the ZK61 Mg alloy significantly. The LCSM observations on the wear tracks are shown in Fig. 7(d) and a significant decrease in the width and depth of the wear tracks is shown in Fig. 7(e). Compared with the width and depth of the wear track of 342 and 79

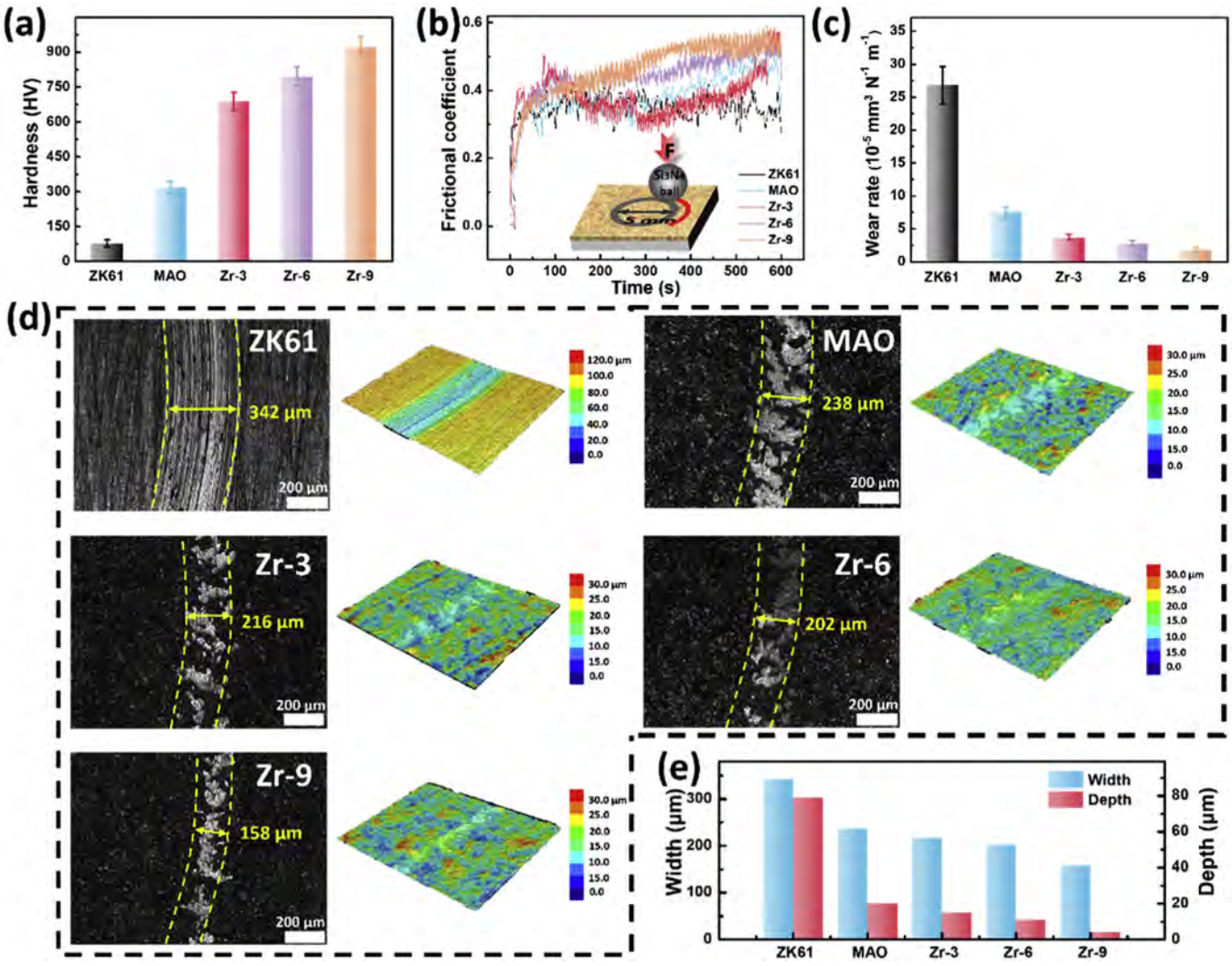


**Fig. 7.** Microhardness and tribological characteristic of the ZK61 Mg alloy and MAO coatings doped with $ZrO_2$ nanoparticles: (a) microhardness, (b) friction coefficients, (c) wear rates (illustrated images of the friction process), (d) LCSM images of the wear tracks and (e) width and depth of the wear tracks.

$\mu$m of the ZK61 Mg alloy, the corresponding values decrease to 158 and 4 $\mu$m for Zr-9, respectively. This observation is consistent with the wear rates and despite a slight increase in the friction coefficient, $ZrO_2$ doping affects the hardness and wear resistance significantly.

To further explore the mechanism of the improved wear properties of the $ZrO_2$ nanoparticles doped MAO coatings, the micromorphology and chemical composition of the wear scars are determined as shown in Figs. 8 and S2. The wear scars on the ZK61 Mg alloy display a typical furrow morphology, indicating severe wear and surface deformation and EDS reveals the accumulation of oxide at the edge of the wear scars arising from oxidation from local heat generation during the friction test (Fig. S2). In comparison, the wear scars on the MAO coating sample show a significant amount of debris and particles, as shown in Fig. 8(a). Some debris undergo delamination and even exfoliation as the protrusions are worn and delaminated by the abrasive ball.

The wear scars of the $ZrO_2$-doped coatings show narrower and flatter tracks with fewer particles, as shown in Fig. 8(b–d), revealing better wear resistance. However, the number of particles inside the wear scars increases with coating hardness and they are more prone to being crushed by the abrasive ball. EDS shows that the wear scars have Mg, O, P, F, and Zr. Zr tends to aggregate on account of the initial clustering of $ZrO_2$ particles in the pores. Overall, the friction tests indicate that the addition of $ZrO_2$ significantly enhances the wear resistance.

**Table 1**
Corrosion potentials and corrosion current densities of the ZK61 Mg alloy and MAO coatings doped with different concentrations of $ZrO_2$ nanoparticles.

| Samples | Corrosion potential (V) | Corrosion current density (A $cm^{-2}$) |
|---|---|---|
| ZK61 | −1.528 | $1.065 \times 10^{-4}$ |
| MAO | −1.437 | $5.051 \times 10^{-6}$ |
| Zr-3 | −1.386 | $1.032 \times 10^{-6}$ |
| Zr-6 | −1.307 | $6.949 \times 10^{-7}$ |
| Zr-9 | −1.184 | $2.234 \times 10^{-7}$ |

### 3.3. Electrochemical properties and immersion tests

Electrochemical tests are conducted on the pristine ZK61 Mg alloy, MAO, Zr-3, Zr-6, and Zr-9 in the 3.5wt% NaCl solution to evaluate the corrosion resistance. The Tafel results in Fig. 9(a) and Table 1 indicate that the corrosion potentials of the ZK61 Mg alloy increase from −1.528 V to −1.437 V after MAO and −1.386, −1.307, and −1.184 V for Zr-3, Zr-6, and Zr-9, respectively. Correspondingly, the corrosion current densities decrease from $1.065 \times 10^{-4}$ A $cm^{-2}$

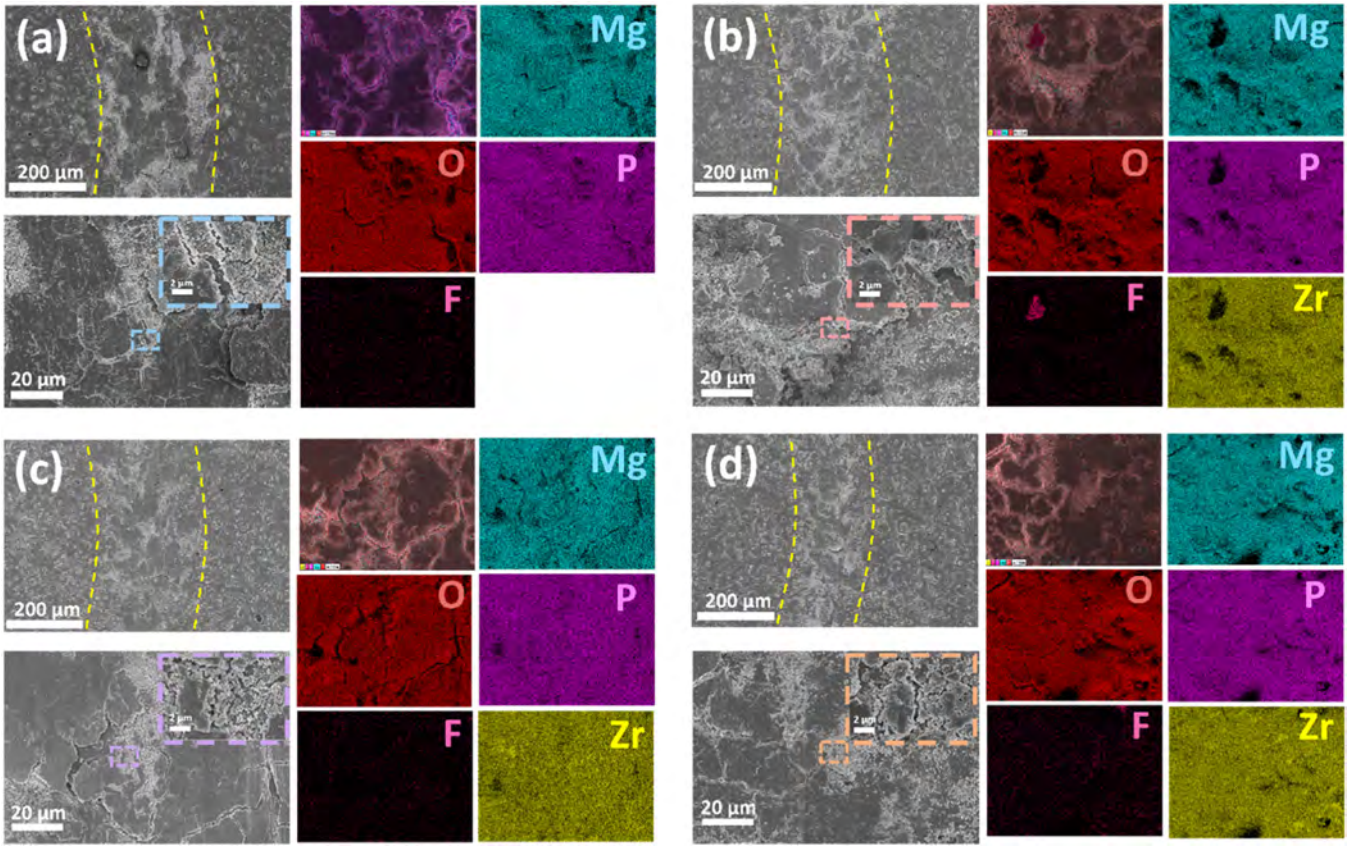


**Fig. 8.** SEM images and EDS maps of the worn surfaces of different samples after the friction test: (a) MAO, (b) Zr-3, (b) Zr-6, and (d) Zr-9.

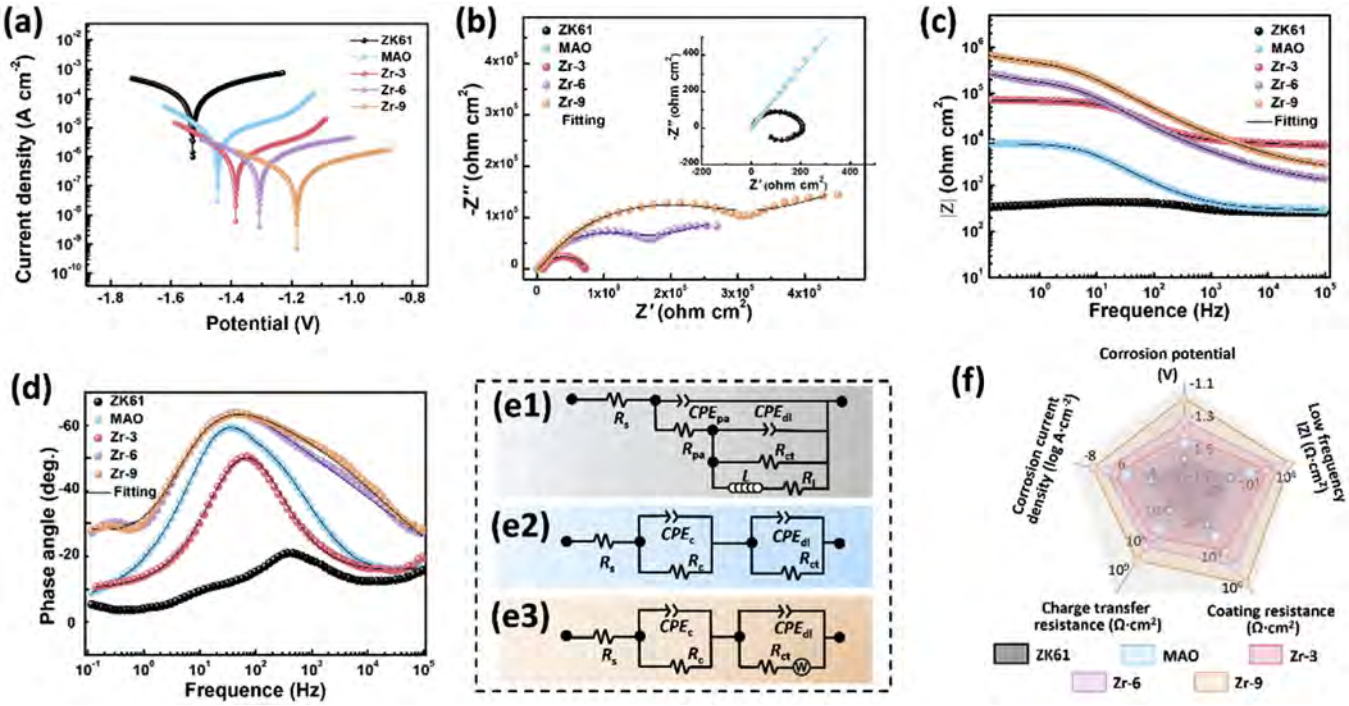


**Fig. 9.** Electrochemical performance of the ZK61 Mg alloy and MAO coatings doped with $ZrO_2$ nanoparticle. (a) Tafel. (b–e) EIS: (b) Nyquist, (c) Bode-impedance, (d) Bode-phase angle, (e) equivalent circuits. (f) Pentagon coordinate graph.

of the ZK61 Mg alloy to 5.051 × $10^{-6}$, 1.032 × $10^{-6}$, 6.949 × $10^{-7}$, and 2.234 × $10^{-7}$ A $cm^{-2}$ of the MAO, Zr-3, Zr-6, and Zr-9 samples, respectively, indicating a decrease in the corrosion current densities of over four orders of magnitude. The improved corrosion resistance can be attributed to the protection provided by the MAO coatings, as well as the sealing effects rendered by the $ZrO_2$ nanoparticles.

EIS is carried out to analyze the corrosion resistance. Fig. 9(b) displays that both the ZK61 Mg alloy and MAO-coated samples exhibit a capacitive behavior during immersion in the salt solution. Compared to the ZK61 Mg alloy, the diameter of the capacitive of the MAO coating increases gradually, especially those doped with $ZrO_2$ nanoparticles, indicating enhanced corrosion resistance. In general, the impedance modulus of the Bode impedance plot at low frequencies reflects the overall impedance of the samples in the corrosion system. As shown in Fig. 9(c), the low-frequency impedance of the MAO coating increases nearly by two orders of magnitude compared to the ZK61 Mg alloy, from 3.431 × $10^2$ Ω $cm^2$ to 8.223 × $10^3$ Ω $cm^2$. Additionally, Zr-3, Zr-6, and Zr-9 exhibit low-frequency resistances of 7.0781 × $10^4$, 2.709 × $10^5$, and 6.782 × $10^5$ Ω $cm^2$ in the salt solution, respectively. Hence, the $ZrO_2$ nanoparticles enhance the corrosion resistance in the salt solution.

The complex nonlinear least squares method is employed to fit the EIS results and obtain an equivalent circuit (EC). According to the time constant in the Bode phase angle in Fig. 9(d), the fitted circuit is depicted in Fig. 9(e). The relaxation processes of the ZK61 Mg alloy at medium-high and low frequencies occur in the surface passivation layer and metal interface, respectively. The capacitive loop in the high-frequency or intermediate frequency range is associated with the MAO coating, while the electrochemical behavior in the low-frequency range is attributed to the interfacial reaction between the coating and substrate in the solution [59]. Due to the rough and porous characteristics of the coating and the non-uniformity of the surface chemical composition, the use of ideal capacitors and resistors to analyze the charge transfer interface processes is hindered. Therefore, a constant phase element (CPE) described by Eq. (2) is selected to express the non-ideal resistive and capacitive behavior of the coating [60]:

$$Z_{CPE} = \frac{1}{T(j\omega)^n}, \quad -1 \le n \le 1 \tag{2}$$

where $Z_{CPE}$ is the resistance of CPE, $T$ represents the CPE coefficient, $n$ is the CPE index, $j = \sqrt{-1}$ represents the imaginary unit, and $\omega$ is the angular frequency. When $n$ is equal to 1, 0 and −1, it is analogous to an ideal capacitor, ideal resistor and ideal inductor, respectively [61]. The EIS of the ZK61 Mg alloy are fitted using the inductance shown in Fig. 9(e1), and MAO, Zr-3 and Zr-6 samples are fitted using the capacitor circuit shown in Fig. 9(e2), respectively, while the Zr-9 coating is fitted with the addition of a Warburg resistor shown in Fig. 9(e3). $R_s$ represents solution resistance. $CPE_c$ and $R_c$ are the capacitance and resistance of the passivation layer or MAO coating of the ZK61 Mg alloy, $CPE_{dl}$ and $R_{ct}$ represent the double-layer capacitance and charge transfer resistance in the Faraday process, and W is the Warburg resistance. $L$ and $R_l$ represent the Inductance and its corresponding resistance. $\chi^2$ represent the chi square distribution of the fitted data.

Table 2 shows the variations of the EC constant element coefficients and resistances of the ZK61 Mg alloy and various coatings in the salt solution. After MAO, $CPE_{dl}$ decreases from 6.688 × $10^{-4}$ $\Omega^{-1}$ $s^n$ $cm^{-2}$ of the ZK61 Mg alloy to 1.862×$10^{-5}$ $\Omega^{-1}$ $s^n$ $cm^{-2}$ of the MAO coating. As increasing $ZrO_2$ concentrations, $CPE_{dl}$ decreases further to 7.884×$10^{-6}$, 1.344×$10^{-6}$, and 2.978×$10^{-7}$ $\Omega^{-1}$ $s^n$ $cm^{-2}$ for Zr-3, Zr-6, and Zr-9, respectively. Meanwhile, $CPE_c$ decreases from 4.998×$10^{-3}$ $\Omega^{-1}$ $s^n$ $cm^{-2}$ of the ZK61 Mg alloy to 6.359×$10^{-4}$, 2.651×$10^{-5}$, 4.226×$10^{-6}$, and 2.644×$10^{-6}$ $\Omega^{-1}$ $s^n$ $cm^{-2}$ for the MAO, Zr-3, Zr-6, and Zr-9 samples, respectively. The change in the resistance is opposite to that of CPE. The resistance $R_{ct}$ increases from 1.673×$10^2$ Ω $cm^2$ of the ZK61 Mg alloy to 6.992×$10^3$ Ω $cm^2$ of the MAO coating. After introduction of $ZrO_2$ nanoparticles, the $R_{ct}$ values of the MAO coatings increase gradually, reaching a maximum of 2.161×$10^6$ Ω $cm^2$ for Zr-9, and $R_c$ exhibits the same increasing trend. Hence, the MAO coating can resist corrosion and infiltration of the salt solution to the Mg alloy by acting as a physical barrier. At the same time, the $ZrO_2$ nanoparticles weaken the charge transfer process of corrosion anions in the salt solution, effectively resisting the corrosion of weak pores by the corrosive medium and significantly enhancing the corrosion resistance in the salt solution. By comparing the electrochemical data of the corrosion potential, corrosion current density, low-frequency resistance, charge transfer resistance, and coating resistance, based on the pentagon coordinate graph, Zr-9 delivers the highest corrosion resistance performance, as shown in Fig. 9(f).

Fig. 10 shows the optical images of the ZK61 Mg alloy without and with MAO coatings immersed in the salt solution for 28 d. After immersion for 1 d, the surface of the ZK61 Mg alloy changes from a metallic luster to gray, and numerous corrosion pores appear from the surface. With prolonged immersion time, corrosion gradually increases, and the pores expand horizontally and vertically. After 28 d, a 1 mm thick layer on the unprotected ZK61 Mg alloy has been penetrated. In contrast, the sample with the MAO coating only shows small corrosion pores after 3 d However, the porous structure results in some penetration of the corrosion medium and local corrosion of the substrate. As the immersion time prolongs, the number of corrosion pores on the MAO sample increases slightly, but the size does not increase significantly. After 28 d, more small local corrosion pores appear from the MAO coating, but the porous structure cannot resist long-term immersion corrosion. In contrast, the corrosion resistance of the MAO coatings doped with $ZrO_2$ nanoparticles increases significantly. Uniform doping with $ZrO_2$ nanoparticles and their aggregation in pores, thus providing high chemical stability. The higher the $ZrO_2$ nanoparticles concentration, the greater the enhancement.

Fig. 11 displays the LCSM pictures of the ZK61 Mg alloy without and with MAO coatings immersed in the salt solution for 28 d Similar to the optical images in Fig. 10, those show the evolution of pitting pores on the ZK61 Mg alloy. Large corrosion pores emerge from the ZK61 Mg alloy surface after 1 d and the size and depth increase gradually with time. Conversely, the MAO, Zr-3, Zr-6, and Zr-9 coated samples show only small corrosion pores after 3, 7, 14, and 28 d. In comparison with the unprotected alloy substrate, the expansion rate of corrosion pores in the coated samples is significantly smaller.

Fig. 12 shows the surface topography and chemical composition of the ZK61 Mg alloy without and with MAO coatings after immersion in the salt solution for 28 d. The ZK61 Mg alloy experiences severe corrosion as shown by the porous surface and cracked corrosion film. The corrosion film has a nanosheet structure typical of $Mg(OH)_2$. Owing to the porous and cracked characteristics of the corrosion film, it is unable to resist $Cl^-$ attack, as shown in Fig. 12(a1–a3). EDS reveals the presence of Mg, O, Zr, and Cl with a chlorine content of 2.34 at.%, indicating poor corrosion resistance of the alloy, as shown in Fig. 12(a4) and Fig. S3. Zn is not present in the corrosion product, while a low content of Zr is observed because the higher potential Mg–Zn second phase at the grain boundaries of the alloy causes preferential micro-galvanic corrosion of α-Mg as the anode. Additionally, a small amount of Zr dissolves in the grains and transforms into $ZrO_2$ during corrosion. After MAO, the samples exhibit localized corrosion. The original volcanic features are replaced by a large area of cracks and some delamination occurs. The corrosive liquid corrodes longitudi-

**Table 2**
Fitted EIS data of the ZK61 Mg alloy and MAO coatings doped with different concentrations of $ZrO_2$ nanoparticles.

| Samples | ZK61 | MAO | Zr-3 | Zr-6 | Zr-9 |
|---|---|---|---|---|---|
| $R_s$ ($\Omega$ cm$^2$) | 18.2 | 20.5 | 21.2 | 22.3 | 19.6 |
| $CPE_c$ ($\Omega^{-1}$ $s^n$ cm$^{-2}$) | $4.998\times10^{-3}$ | $6.359 \times 10^{-4}$ | $2.651 \times 10^{-5}$ | $4.226 \times 10^{-6}$ | $2.644 \times 10^{-6}$ |
| $n_c$ | 0.6747 | 0.5344 | 0.8509 | 0.876 | 0.2572 |
| $R_c$ ($\Omega$ cm$^2$) | 174 | $1.034 \times 10^3$ | $9.023 \times 10^3$ | $5.107 \times 10^4$ | $4.077 \times 10^5$ |
| $W$ (S $s^{0.5}$ cm$^{-1}$) | – | – | – | – | $1.751 \times 10^{-6}$ |
| $CPE_{dl}$ ($\Omega^{-1}$ $s^n$ cm$^{-2}$) | $6.688 \times 10^{-4}$ | $1.862 \times 10^{-5}$ | $7.884 \times 10^{-6}$ | $1.344 \times 10^{-6}$ | $2.978 \times 10^{-7}$ |
| $n_{dl}$ | 0.8871 | 0.8562 | 0.1918 | 0.4367 | 0.8332 |
| $R_{ct}$ ($\Omega$ cm$^2$) | 167.3 | $6.992 \times 10^3$ | $7.12 \times 10^4$ | $4.545 \times 10^5$ | $2.161 \times 10^6$ |
| $L$ (H cm$^2$) | 16.78 | – | – | – | – |
| $R_l$ ($\Omega$ cm$^2$) | 94.47 | – | – | – | – |
| $\chi^2$ | $4.5 \times 10^{-4}$ | $9.9 \times 10^{-4}$ | $3.6 \times 10^{-4}$ | $6.2 \times 10^{-4}$ | $5.6 \times 10^{-4}$ |

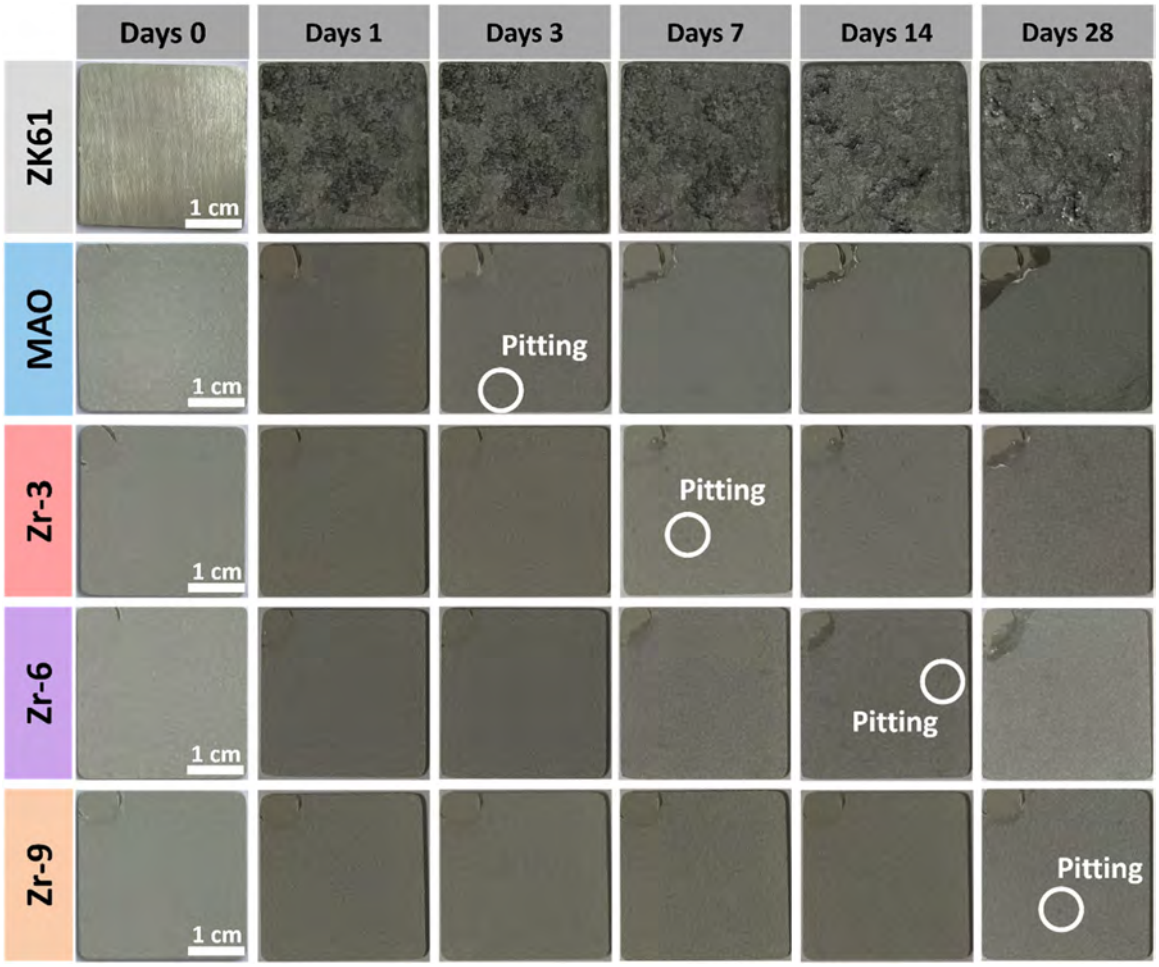


**Fig. 10.** Optical images of the ZK61 Mg alloy and MAO coatings doped with $ZrO_2$ nanoparticles after immersion in the salt solution for 0, 1, 3, 7, 14, and 28 d.

nally along the surface pores, and the production of $H_2$ and formation of porous corrosion products crack the coating subsequently reducing the corrosion resistance, as shown in Fig. 12(b1–b3). EDS reveals the presence of Mg, O, P, F, and Cl in the corrosion product, but the Cl concentration decreases to 1.05 at.%, furnishing proof of the improved properties stated in Figs. 12(b4) and S4.

After doping with $ZrO_2$ nanoparticles, the corrosion resistance of Zr-3 improves and the size of the local corrosion pits decreases. These pits are occupied by corrosion products and cracked coatings. Further examination reveals that the corrosion product has a nanofibrous structure, which is denser than the lamellar corrosion product, as shown in Fig. 12(c1–c3). The denser structure can be attributed to the inclusion of a small amount of $ZrO_2$ which possesses higher chemical stability and fills the porous $Mg(OH)_2$ structure to enhance film densification. Film densification is commonly assessed using PBR, which is determined by the ratio of the compound volume ($V_{com}$) to metal volume ($V_M$) as shown in Eq. (3):

$$PBR = \frac{V_{com}}{V_M} = \frac{M_{com} \cdot \rho_M}{n \cdot A \cdot \rho_{com}} \quad (3)$$

where $M_{com}$ and $\rho_{com}$ represent the molar mass and densification of the compound, $A$ and $\rho_M$ are the atomic mass and densification of the metal, and $n$ is the number of metal atoms in the molecule [62,63]. When the PBR of the corrosion product is <1, it is generally considered to be structurally loose and unable to provide effective corrosion protection. If it is in the range of 1–2, the surface layer is generally considered to be relatively dense with good corrosion protection properties [64]. Therefore, based on the PBR

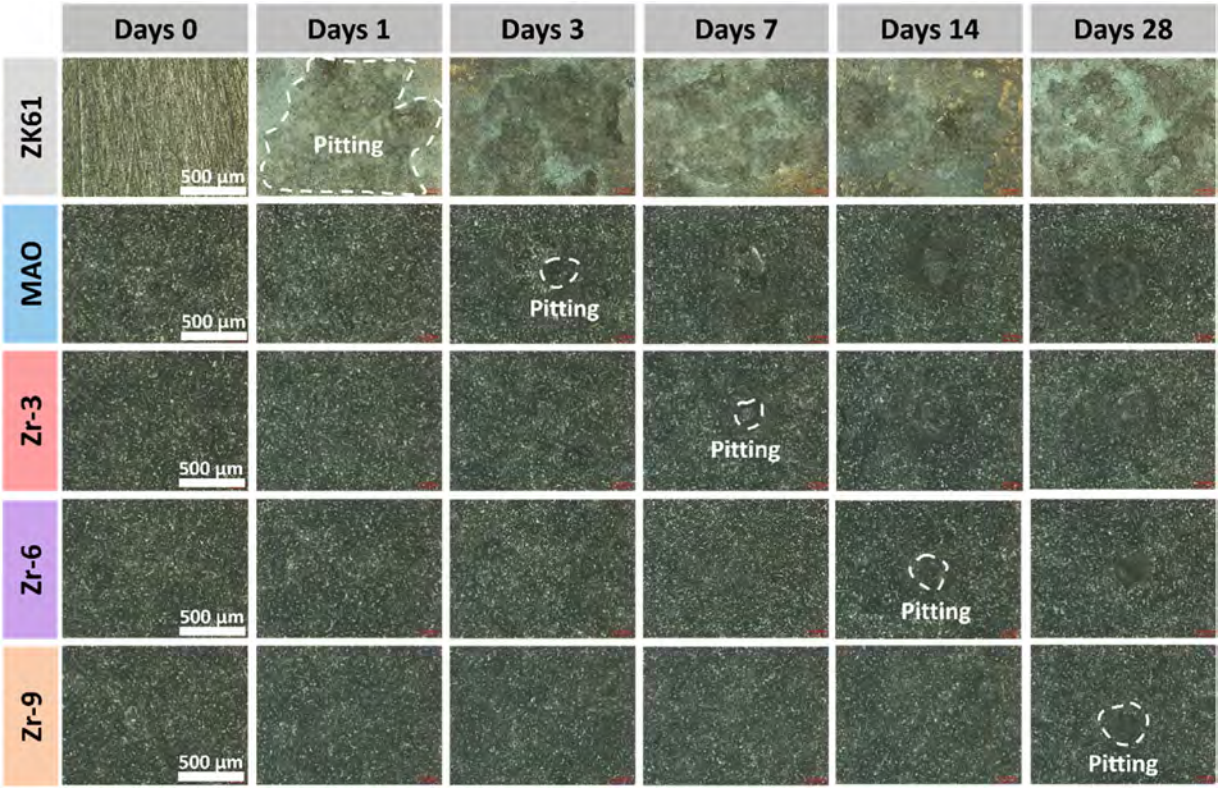


**Fig. 11.** LCSM images of the ZK61 Mg alloy and MAO coatings doped $ZrO_2$ nanoparticle after immersion in the salt solution for 0, 1, 3, 7, 14, and 28 d.

of the corrosion layer for general MAO coatings, the main corrosion product is $MgO/Mg(OH)_2$, which has a PBR of about 0.81 [65], while the PBR of $ZrO_2$ is 1.56 [66]. Consequently, when $ZrO_2$ is incorporated into the $MgO/Mg(OH)_2$ corrosion layer, the overall PBR of the film layer will increase. In addition, the higher the doping concentration, the better the densification. The EDS analysis of the corrosion products on Zr-3 shows that the corrosion product layer mainly contains Mg, O, P, F, Zr, and Cl and the Cl concentration of 0.27 at.% is less than that in MAO sample. The Zr concentration is 2.36 at.%, suggesting that after corrosion occurs, the locally stable $ZrO_2$ plays an effective role in improving the densification of the corrosion layer, as shown in Fig. 12(c4) and Fig. S5.

The corrosion resistance of the coating doped with a larger concentration of $ZrO_2$ increases. Zr-6 shows only small corroded areas and the cracks surrounding the corrosion pits are minimal in size and range. The corrosion film layer shows good densification, and the corrosion product has a nanoscale flocculent or granular structure, as shown in Fig. 12(d1–d3). EDS shows that the corrosion product layer consists of Mg, O, P, F, Zr, and Cl and the Cl concentration decreases further to 0.09 at.%, as shown in Figs. 12(d4) and S6, while the Zr concentration increases to 3.62 at.%, revealing that more $ZrO_2$ is incorporated into the corrosion layer. In comparison, Zr-9 with the largest $ZrO_2$ content shows only localized corrosion at the volcano-like areas after immersion in conjunction with minimal surface cracking. The SEM images show that the corroded areas have nanoscale particles and the corrosion product layer is more compact, as shown in Fig. 12(e1–e3). As shown in Figs. 12(e4) and S7, Mg, O, P, F, and Zr are present and only trace Cl is detected, while the Zr concentration increases to 5.67 at.%.

The cross-sectional SEM images of the corroded samples in Fig. 13 show that the corrosive solution nearly breaches the corrosion film after 28 d. The corrosion product has a nanoscale layered structure as shown in Fig. 13(a). In contrast, the corrosion product consisting of small nanoscale flakes on the MAO sample accumulates on the inner walls of the pores. In some regions, the corrosion layer begins to peel off, as shown in Fig. 13(b) as the long-term attack by $Cl^-$ of the pores converts $Mg(OH)_2$ into soluble $MgCl_2$. However, the $ZrO_2$ nanoparticles reduce pore corrosion, as shown in Fig. 13(c, d), and densification of the corrosion product layer increases gradually with $ZrO_2$ concentration (Fig. 13(e)). The corrosion product gradually morphs into smaller nanoscale particles and the $ZrO_2$ nanoparticles are incorporated into the corrosion product layer. It fills the loose structure of $Mg(OH)_2$, subsequently enhancing the densification of the corrosion layer and improving the corrosion resistance.

### *3.4. Influence of $ZrO_2$ nanoparticles on corrosion properties of the MAO coatings*

According to previous studies [67,68], corrosion of Mg alloys is related to the chemical composition, microstructure, phase precipitation, and morphology. In this study, MAO coatings doped with $ZrO_2$ nanoparticles are fabricated on the ZK61 Mg alloy, and $ZrO_2$ nanoparticles play an important role in improving the corrosion resistance. The corrosion behavior of the bare ZK61 Mg alloy in the salt solution can be divided into three stages, as illustrated in Fig. 14(a). Firstly, the active Mg reacts with water in the corrosive solution to produce a porous $Mg(OH)_2$ layer. At the grain boundaries, the potential of the Mg–Zn second phase is more noble than that of $\alpha$-Mg and micro-galvanic corrosion occurs between them in the corrosive medium to accelerate corrosion and form localized pitting. In the micro-galvanic corrosion process, $\alpha$-Mg, which has a more negative potential, acts as the anode and releases electrons to form $Mg^{2+}$. On the other hand, the Mg–Zn second phase acts as the cathode and absorbs electrons, resulting in the deposition of $H_2$ on the surface. The high local concentrations of $Mg^{2+}$ and $OH^-$ react to form $Mg(OH)_2$, which precipitates on the alloy. This corrosion reaction is represented by Eq. (4) [69]:

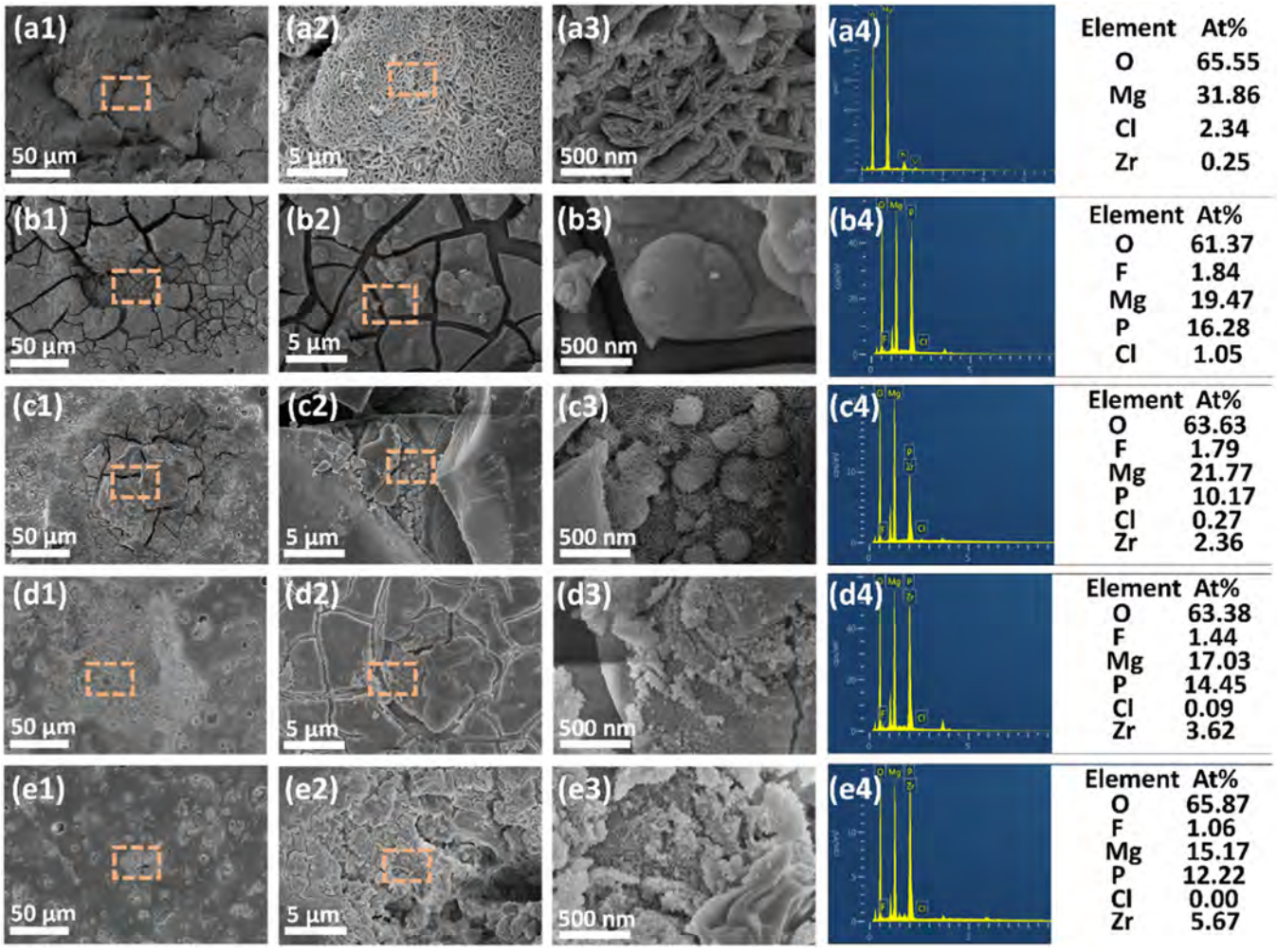


**Fig. 12.** SEM images and EDS spectra of the different samples after immersion in the salt solution for 28 d: (a) ZK61 Mg alloy, (b) MAO, (c) Zr-3, (d) Zr-6, and (e) Zr-9.

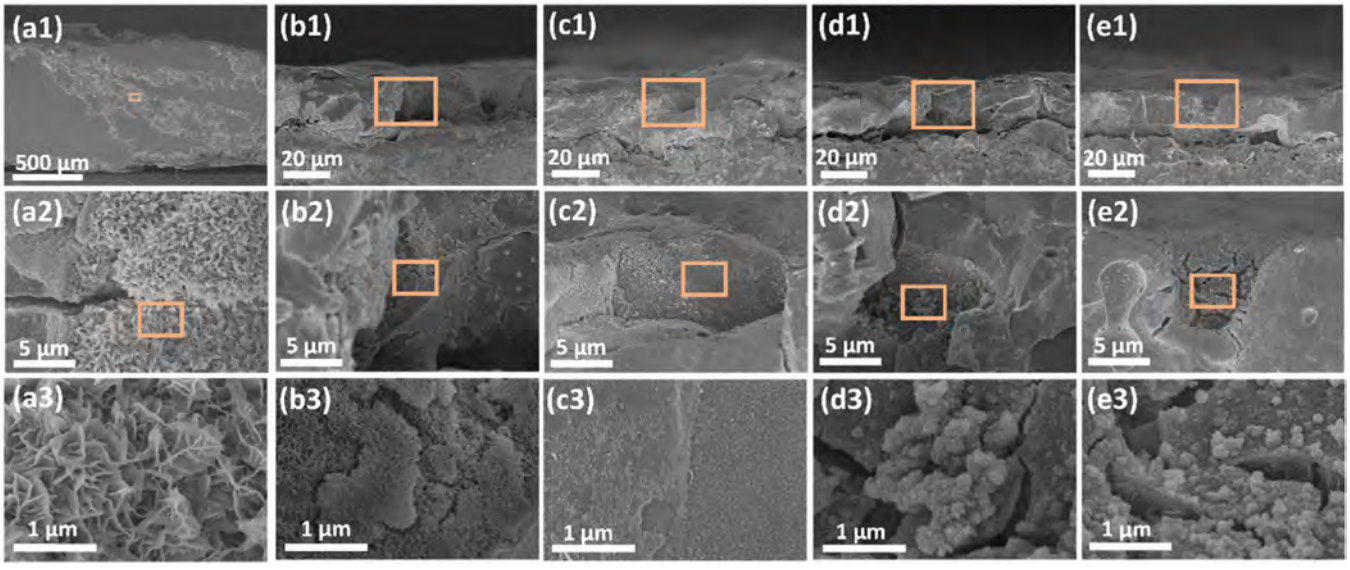


**Fig. 13.** Cross-sectional SEM images of the different samples after immersion in the salt solution for 28 d: (a) ZK61 Mg alloy, (b) MAO, (c) Zr-3, (d) Zr-6, and (e) Zr-9.

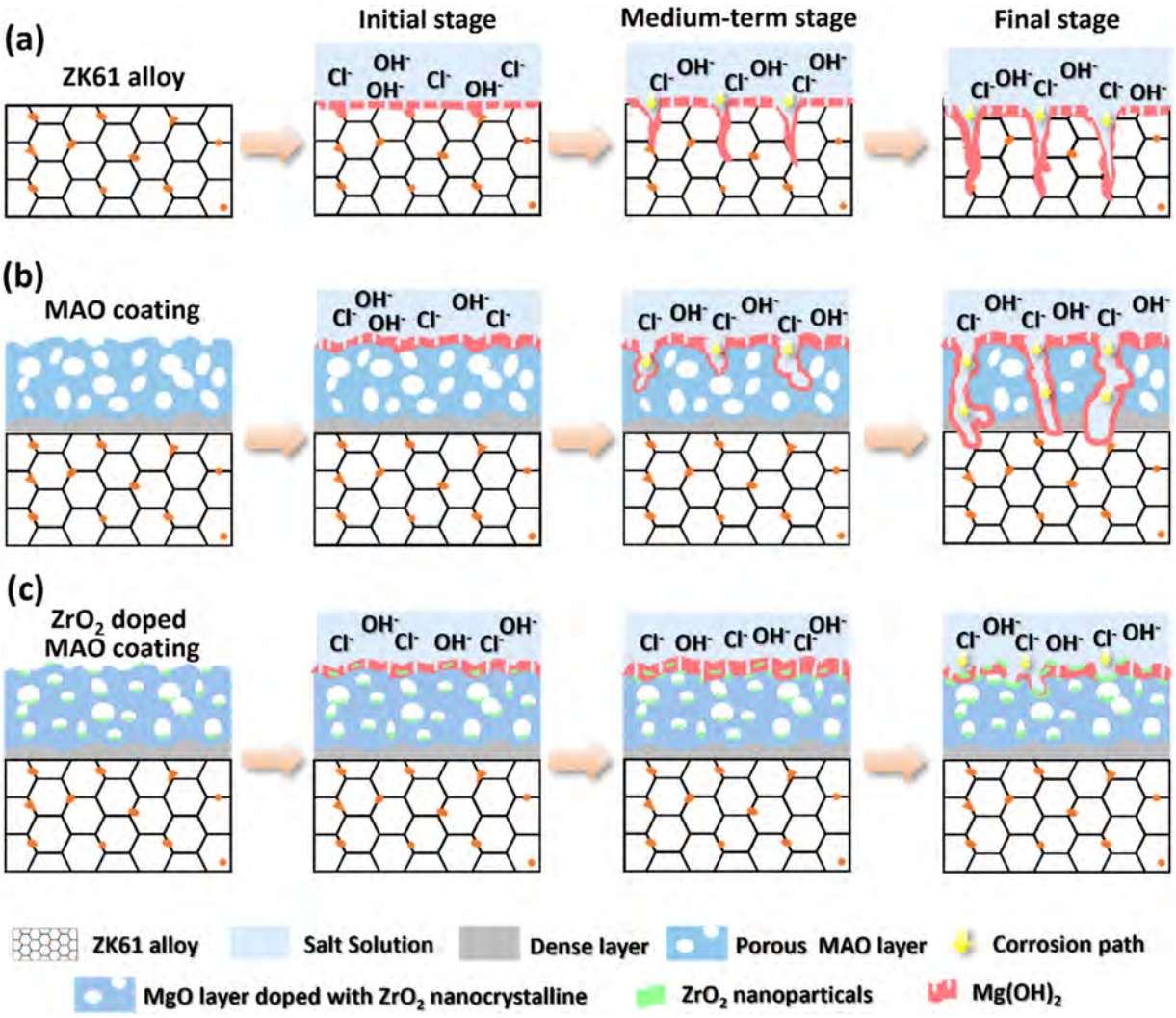


**Fig. 14.** Schematic illustration of the corrosion mechanism of (a) ZK61 Mg alloy, (b) MAO coating, and (c) $ZrO_2$-doped MAO coating in the salt solution.

$$Mg + 2H_2O \rightarrow Mg(OH)_2 + H_2\uparrow \quad (4)$$

The high dissolution rate of $\alpha$-Mg and formation rate of $H_2$ result in a more porous structure of the corrosion product of $Mg(OH)_2$. As the local pH goes up, $Cl^-$ corrodes $Mg(OH)_2$ (Solubility product constant, $K_{sp} = 1.8 \times 10^{-11}$) and converts it into the more soluble compound $MgCl_2$ ($K_{sp} = 54.6$) [70,71], as expressed by Eq. (5) [72]:

$$Mg(OH)_2 + 2Cl^- \rightarrow MgCl_2 + 2OH^- \quad (5)$$

Subsequently, the dissolution of $MgCl_2$ leads to the formation of larger corrosion pores that provide more pathways for the penetration of the corrosive medium. The coupled process involving the corrosion reaction of the Mg substrate and dissolution of corrosion products accelerates the corrosion of the alloy. Therefore, it is crucial to prevent or delay the permeation of the corrosive medium.

A denser coating composed of $MgO/Mg_3(PO_4)_2$ is deposited on the ZK61 Mg alloy by MAO to block the direct contact between the corrosive solution and substrate, as shown in Fig. 14(b). The primary constituent of the MAO coating is MgO, which is more inert than pure Mg, but it is still susceptible to corrosion as expressed by Eq. (6) [73]:

$$MgO + H_2O \rightarrow Mg(OH)_2 \quad (6)$$

Because gas is not released, the corrosion product is relatively compact compared to the ZK61 Mg alloy. However, there are pores in the MAO coating. In a long-term corrosive environment, the corrosive solution penetrates these pores, resulting in pitting at the coating/substrate interface. At weaker pores, the corrosion product $Mg(OH)_2$ increases the pH in the local microenvironment, while $Cl^-$ promotes the transformation of $Mg(OH)_2$ into the more soluble $MgCl_2$ (Eq. (5)). As $MgCl_2$ dissolves, the corrosion product layer is destroyed followed by the formation of pits that expose the underlying region. Consequently, corrosion extends into deeper regions. As MgO in the coating continues to form $Mg(OH)_2$, it is converted into $MgCl_2$ and dissolves. The continuous corrosion connects the internal pores and accelerates corrosion. Eventually, the corrosive solution infiltrates the interface between the MAO coating and alloy to cause rapid pitting corrosion.

The $ZrO_2$ nanoparticles in the MAO coatings improve the corrosion resistance by sealing and secondary strengthening effects. The aggregated $ZrO_2$ nanoparticles in pores block the penetration of the corrosion medium to yield the sealing effect, as shown in Fig. 14(c). Moreover, the uniformly distributed $ZrO_2$ nanoparticles in the MAO coatings enhance the densification of the corrosion product layer to realize the secondary strengthening effect. Owing to local discharges, the $ZrO_2$ nanoparticles re-melt and re-crystallize to form a coating comprising dispersed phases of $MgO/Mg_3(PO_4)_2/ZrO_2$. Similar to the undoped MAO coating, the

relatively active MgO corrodes in the solution, as shown in Eq. (6), to produce the porous $Mg(OH)_2$ corrosion product. However, since the $ZrO_2$ nanocrystals are uniformly distributed in the coating and stable in the corrosive medium, they do not degrade. Therefore, when the nearby MgO reacts to form a porous $Mg(OH)_2$ corrosion product, $ZrO_2$ fills in to enhance the PBR of the film. The higher the $ZrO_2$ concentration, the better the densification efficiency. In the porous areas, the corrosion-resistant film is still corroded by $Cl^-$ and converted into soluble $MgCl_2$. However, in cases of pitting, the $ZrO_2$ redeposits onto the newly formed pits to act as a self-sealing corrosion barrier. As a result, the weak pores are protected and further pitting at the coating/alloy interface is delayed.

## 4. Conclusion

MAO coatings are prepared on the ZK61 Mg alloy in a phosphate electrolyte doped with $ZrO_2$ nanoparticles. The $ZrO_2$ nanoparticles are incorporated into the coatings without ablation by designing the $MgF_2$ passivation layer, and are dispersed evenly in the MAO coatings to form nanocrystals *via* re-melting and precipitation. The doped coatings have higher hardness, as exemplified by a hardness of 79 HV of the ZK61 Mg alloy to 924 HV of Zr-9 coating. Furthermore, the wear rate decreases from $2.68\times10^{-4}$ $mm^3$ $N^{-1}$ $m^{-1}$ of the ZK61 Mg alloy substrate to $1.84\times10^{-5}$ $mm^3$ $N^{-1}$ $m^{-1}$ of Zr-9 coating. Electrochemical tests confirm the enhanced corrosion resistance by the MAO coatings doped with $ZrO_2$ nanoparticles. Compared with the bare ZK61 Mg alloy substrate, $ZrO_2$ in the MAO coating increases the corrosion potentials from −1.528 V to −1.184 V, decreases the corrosion current densities from $1.065\times10^{-4}$ A $cm^{-2}$ to $3.960\times10^{-8}$ A $cm^{-2}$, and increases the charge transfer resistance from $3.41\times10^2$ Ω $cm^2$ to $6.782\times10^5$ Ω $cm^2$. Immersion tests conducted in a salt solution for 28 d reveal severe corrosion on the bare ZK61 Mg alloy, whereas Zr-9 shows only minor corrosion. The improvement stems from the inert properties of $ZrO_2$, which fills the looser structure of the $Mg(OH)_2$ corrosion product film and improves the densification of the corrosion product film. By incorporating $ZrO_2$ into MAO coatings, the wear resistance and corrosion resistance of the ZK61 Mg alloy can be improved simultaneously and the materials have large commercial potential.

## Declaration of competing interest

The authors declare that they have no known competing financial interests or personal relationships that could have appeared to influence the work reported in this paper.

## CRediT authorship contribution statement

**Chao Yang:** Writing – original draft, Investigation, Funding acquisition, Conceptualization. **Chenyu Wang:** Software, Resources, Data curation. **Zhao Shen:** Visualization, Investigation, Formal analysis. **Liping Zhou:** Supervision, Methodology, Formal analysis. **Liyuan Sheng:** Writing – review & editing, Investigation, Funding acquisition. **Daokui Xu:** Visualization, Validation, Methodology, Investigation. **Yufeng Zheng:** Writing – review & editing, Visualization, Investigation, Conceptualization. **Paul K. Chu:** Writing – review & editing, Funding acquisition, Conceptualization. **Shu Xiao:** Supervision, Formal analysis, Investigation, Writing – review & editing. **Tao Ying:** Validation, Methodology, Formal analysis. **Xiaoqin Zeng:** Writing – review & editing, Investigation.

## Acknowledgments

This work was financially supported by the Postdoctoral Fellowship Program of CPSF (No. GZC20231545), the China Postdoctoral Science Foundation (Nos. 2024T170557 and 2023M742224), the Shanghai Post-doctoral Excellence Program (No. 2023440), the National Natural Science Foundation of China (Nos. 52127801, 52401101, and 22205012), the Shenzhen Basic Research Project (Nos. JCYJ20210324120001003 and JCYJ20200109144608205), the Guangdong Basic and Applied Basic Research Foundation (Nos. 2020A1515011301 and 2021A1515012246), the IER Foundation (Nos. IERF202201 and IERF202202), the City University of Hong Kong Donation Research (No. DON-RMG 9229021), the Hong Kong PDFS - RGC Postdoctoral Fellowship Scheme (Nos. PDFS2122–1S08 and CityU 9061014), and the Hong Kong HMRF (Health and Medical Research Fund) (Nos. 2120972 and CityU 9211320).

## Supplementary materials

Supplementary material associated with this article can be found, in the online version, at doi:10.1016/j.jmst.2024.10.023.

## References

[1] Z.P. Wang, Z. Shen, Y. Liu, Y.H. Zhao, Q.C. Zhu, Y.W. Chen, J.Y. Wang, Y.X. Li, S. Lozano-Perez, X.Q. Zeng, J. Magnes. Alloy. 12 (2024) 4045–4052.
[2] C.Y. Wang, M.S. Sun, C. Yang, H.Y. Wang, J. Wang, L. Mao, Y. Yang, T. Ying, P.K. Chu, X.Q. Zeng, J. Magnes. Alloy. (2024), doi:10.1016/j.jma.2024.05.012.
[3] D.X. Gao, Z. Shen, K. Chen, X. Zhou, H. Liu, J.Y. Wang, Y.X. Li, Z.X. Liu, H.Q. Deng, W.Y. Wang, X.Q. Zeng, Prog. Mater. Sci. 147 (2025) 101348.
[4] H. Zhang, J.Y. Zhao, R.G. Li, B.S. Liu, S.S. Li, S. Sha, Y.H. Zhang, M. Xu. Y. Tang, Acta. Metall. Sin.-Engl. Lett. 37 (2024) 1367–1376.
[5] D. Cai, X. Zhao, L. Yang, R. Wang, G. Qin, D. Chen, E. Zhang, J. Mater. Sci. Technol. 81 (2021) 13–25.
[6] R.C. Zeng, J. Zhang, W.J. Huang, W. Dietzel, K.U. Kainer, C. Blawert, W. Ke, Trans. Nonferrous Met. Soc. China 16 (2006) S763–S771.
[7] Y. Lv, Y.P.g Zhang, X. Liu, Z.H. Dong, X.R. Zhou, X.X. Zhang, Acta. Metall. Sin.-Engl. Lett. 37 (2024) 665–677.
[8] L. Sun, H. Ma, C. Guan, J. Wang, P. Zhang, P. Jin, F. Wei, Y. Peng, Corros. Sci. 208 (2022) 110610.
[9] Z.Y. Ding, L.Y. Cui, R.C. Zeng, Y.B. Zhao, S.K. Guan, D.K. Xu, C.G. Lin, J. Mater. Sci. Technol. 34 (2018) 1550–1557.
[10] Y.Y. Chen, T. Ying, Y. Yang, J.Y. Wang, X.Q. Zeng, Corros. Sci. 216 (2023) 111106.
[11] W.H. Yao, L. Wu, J.F. Wang, B. Jiang, D.F. Zhang, M. Serdechnova, T. Shulha, C. Blawert, M.L. Zheludkevich, F.S. Pan, J. Mater. Sci. Technol. 118 (2022) 158–180.
[12] E. Rocca, C. Juers, J. Steinmetz, Corros. Sci. 52 (2010) 2172–2178.
[13] R. Kara, H. Zengin, Acta Metall. Sin.-Engl. Lett. 35 (2022) 1195–1206.
[14] M. Daavari, M. Atapour, M. Mohedano, H.M. Sánchez, J. Rodríguez-Hernández, E. Matykina, R. Arrabal, A. Taherizadeh, J. Magnes. Alloy. 10 (2022) 3217–3233.
[15] J.M. Zhao, X. Xie, C. Zhang, Corros. Sci. 114 (2016) 146–155.
[16] Y.W. Song, K.H. Dong, D.Y. Shan, E.H. Han, J. Magnes. Alloy. 1 (2013) 82–87.
[17] Z.Y. Ding, L.Y. Cui, X.B. Chen, R.C. Zeng, S.K. Guan, S.Q. Li, F. Zhang, Y.H. Zou, Q.Y. Liu, J. Alloy. Compd. 764 (2018) 250–260.
[18] M. Sun, A. Yerokhin, M.Y. Bychkova, D.V. Shtansky, E.A. Levashov, A. Matthews, Corros. Sci. 111 (2016) 753–769.
[19] L.Y. Cui, H.P. Liu, W.L. Zhang, Z.Z. Han, M.X. Deng, R.C. Zeng, S.Q. Li, Z.L. Wang, J. Mater. Sci. Technol. 33 (2017) 1263–1271.
[20] A. Ghanbari, A. Bordbar-Khiabani, F. Warchomick, C. Sommitsch, B. Yarmand, A. Zamanian, Surf. Interfaces 36 (2023) 102495.
[21] T. Hu, Y.J. Ouyang, Z.H. Xie, L. Wu, J. Mater. Sci. Technol. 92 (2021) 225–235.
[22] Y.Q. Li, Y.J. Ouyang, R. Fang, X. Jiang, Z.H. Xie, L. Wu, J.L. Long, C.J. Zhong, Chem. Eng. J. 430 (2022) 132776.
[23] R.J. Liu, D. Xu, Y. Liu, L. Wu, Q.W. Yong, Z.H. Xie, Ceram. Int. 49 (2023) 30039–30048.
[24] F. Singer, M. Schlesak, C. Mebert, S. Hohn, S. Virtanen, ACS Appl. Mater. Interfaces 7 (2015) 26758–26766.
[25] Y. Shu, F. Peng, Z.H. Xie, Q.W. Yong, L. Wu, J.N. Xie, M. Li, J. Magnes. Alloy. 12 (2024) 3292–3307.
[26] D. Xu, Z.Z.L. Zhuo, Z.H. Xie, Q.W. Yong, L. Wu, C.J. Zhong, Corros. Sci. 236 (2024) 112229.
[27] W.C. Gu, W.B. Li, Y. Zhang, Y.G. Xia, Q.L. Wang, W. Wang, P. Liu, X.Q. Yu, H. He, C.H. Liang, Y.X. Ban, C.W. Mi, S. Yang, W. Liu, M.M. Cui, X. Deng, Z.K. Wang, Y.F. Zhang, Nat. Commun. 14 (2023) 5953.
[28] S.Y. Wang, N.C. Si, Y.P. Xia, L. Liu, Trans. Nonferrous Met. Soc. China 25 (2015) 1926–1934.
[29] C. Yang, J. Huang, S.H. Cui, R.K.Y. Fu, L.Y. Sheng, D.K. Xu, X.B. Tian, Y.F. Zheng, P.K. Chu, Z.Z. Wu, J. Magnes. Alloy. 12 (2024) 3602–3615.
[30] J. Liang, P.B. Srinivasan, C. Blawert, W. Dietzel, Corros. Sci. 51 (2009) 2483–2492.
[31] S.Y. Wang, Y.P. Xia, L. Liu, N.C. Si, Ceram. Int. 40 (2014) 93–99.
[32] F. Muhaffel, H. Cimenoglu, Surf. Coat. Technol. 357 (2019) 822–832.
[33] Z.Y. Ding, L.Y. Cui, X.B. Chen, R.C. Zeng, S.K. Guan, S.Q. Li, F. Zhang, Y.H. Zou, Q.Y. Liu, J. Alloy. Compd. 764 (2018) 250–260.
[34] Y.L. Zhang, F. Chen, Y. Zhang, C.W. Du, Tribol. Int. 146 (2020) 106135.
[35] X. Li, X. Liu, B.L. Luan, Appl. Surf. Sci. 257 (2011) 9135–9141.

[36] P. Zhang, X. Nie, H. Hu, Y. Liu, Surf. Coat. Technol. 205 (2010) 1508–1514.
[37] B.L. Jiang, Y.F. Ge, in: Corrosion Prevention of Magnesium Alloys, Woodhead Publishing Limited, 2013, pp. 163–196.
[38] S. Lu, Z.X. Wang, J. Chen, X.S. Zhou, Trans. Nonferrous Metals Soc. China 21 (2011) 929–935.
[39] J. Liang, B. Guo, J. Tian, H. Liu, J. Zhou, W. Liu, T. Xu, Surf. Coat. Technol. 199 (2005) 121–126.
[40] C. Yang, L.Y. Sheng, C.C. Zhao, P.H. Chen, W.T. Ouyang, D.K. Xu, Y.F. Zheng, P.K. Chu, J. Mater. Res. Technol. 33 (2024) 2275–2291.
[41] U. Zondiner, A. Rozen, D. Rodan-Legrain, Y. Cao, R. Queiroz, T. Taniguchi, K. Watanabe, Y. Oreg, F. von Oppen, Ady Stern, E. Berg, P. Jarillo-Herrero, S. Ilani, Nature 582 (2020) 203–208.
[42] Y.L. Zhang, F. Chen, Y. Zhang, C.W. Du, Tribol. Int. 146 (2020) 106135.
[43] J.M. Zhao, X. Xie, C. Zhang, Corros. Sci. 114 (2017) 146–155.
[44] B. Diana, A. Erdemir, A.V. Sumant, Mater. Today. 17 (2014) 31–42.
[45] Y. Gao, L.F. Zhao, X.H. Yao, R.Q. Hang, X.Y. Zhang, B. Tang, Surf. Coat. Technol. 349 (2018) 434–441.
[46] C. Yang, M.S. Sun, A.H. Huang, P.H. Chen, P.K. Chu, Ceram. Int. 50 (2024) 46018–46031.
[47] Y.J. Wu, C. Xu, F.Y. Zheng, Mater. Charact. 79 (2013) 93–99.
[48] J.D. Robson, C. Paa-Rai, Acta Mater. 95 (2015) 10–19.
[49] Y.H. Zhao, Y.X. Bai, J. Yang, Y.F. Shen, Y.X. Lou, K. Zhang, Y.H. Wu, Y.X. Li, J. Li, Z.X. Cui, T.G. Wei, S. Ma, Z. Shen, H. Wang, X.Q. Zeng, Corros. Sci. 239 (2024) 112379.
[50] Z.U. Rehman, D.J. Choi, J. Magnes. Alloy. 7 (2019) 555–565.
[51] F. Tjiang, L.W. Ye, Y.J. Huang, C.C. Chou, D.S. Tsai, Ceram. Int. 43 (2017) 67–72.
[52] V. Ezhilselvi, J. Nithin, J.N. Balaraju, S. Subramanian, Surf. Coat. Technol. 288 (2016) 221–229.
[53] A.B. Khiabani, B. Yarmand, M. Mozafari, Surf. Coat. Technol. 360 (2019) 153–171.
[54] A. Apelfeld, B. Krit, V. Ludin, N. Morozova, B. Vladimirov, R.Z. Wu, Surf. Coat. Technol. 322 (2017) 127–133.
[55] L.Y. Sheng, J.T. Guo, T.F. Xi, B.C. Zhang, H.Q. Ye, Prog. Nat. Sci.: Mater. Int. 22 (2012) 231–236.
[56] W.Y. Zhang, Y.H. Du, P. Zhang, J. Magnes. Alloy. 10 (2022) 2460–2474.
[57] F.P. Huo, Y.A. Shen, S.L. He, K.K. Zhang, H. Nishikawa, Vacuum 191 (2021) 110370.
[58] L. Fu, B.H. Wang, W. Xia, Ceram. Int. 48 (2022) 27097–27105.
[59] H. Yan, J.C. Wang, M. Cai, X. Wang, S.J. Song, X.Q. Fan, L. Zhang, H. Li, W. Li, M.H. Zhu, Corros. Sci. 174 (2020) 108813.
[60] D. Wang, P. Zhou, Y. Zhang, T. Zhang, F.H. Wang, Corros. Sci. 222 (2023) 111428.
[61] A. Jangde, S. Kumar, C. Blawert, Corros. Sci. 157 (2019) 220–246.
[62] J. Gray, B. Luan, J. Alloy. Compd. 336 (2002) 88–113.
[63] C. Yang, H. Cai, S.H. Cui, J. Huang, J.Y. Zhu, Z.C. Wu, Z.Y. Ma, R.K.Y. Fu, L.Y. Sheng, X.B. Tian, P.K. Chu, Z.Z. Wu, Surf. Coat. Technol. 433 (2022) 128148.
[64] C.H. Xu, W. Gao, Mater. Res. Innov. 3 (2000) 231–235.
[65] R.C. Zeng, E.H. Han, W. Ke, Int. J. Fatigue 36 (2012) 40–46.
[66] L. Gosmain, C. Valot, D. Ciosmak, O. Sicardy, Solid State Ionics 633 (2001) 141–142.
[67] B.J. Wang, D.K. Xu, X. Cai, Y.X. Qiao, L.Y. Sheng, J. Magnes. Alloy. 9 (2021) 560–568.
[68] A. Fattah-alhosseini, R. Chaharmahali, K. Babaei, J. Magnes. Alloy. 10 (2022) 1171–1190.
[69] A.P. Loperena, S.B. Saidman, I.L. Lehr, Corros. Commun. 14 (2024) 11–22.
[70] F. Gong, J. Shen, R. Gao, X. Xie, X. Luo, Appl. Surf. Sci. 365 (2016) 268–274.
[71] R.C. Zeng, X.T. Li, S.Q. Li, F. Zhang, E.H. Han, Sci. Rep. 43 (2015) 13026.
[72] H.X. Wang, Y.W. Song, D.Y. Shan, E.H. Han, Corros. Commun. 2 (2021) 24–32.
[73] C.Q. Li, B.B. Deng, L.J. Dong, B.Q. Shi, Y. Dong, F. Peng, Z.R. Zhang, Mater. Des. 221 (2022) 111019.

# Supporting information

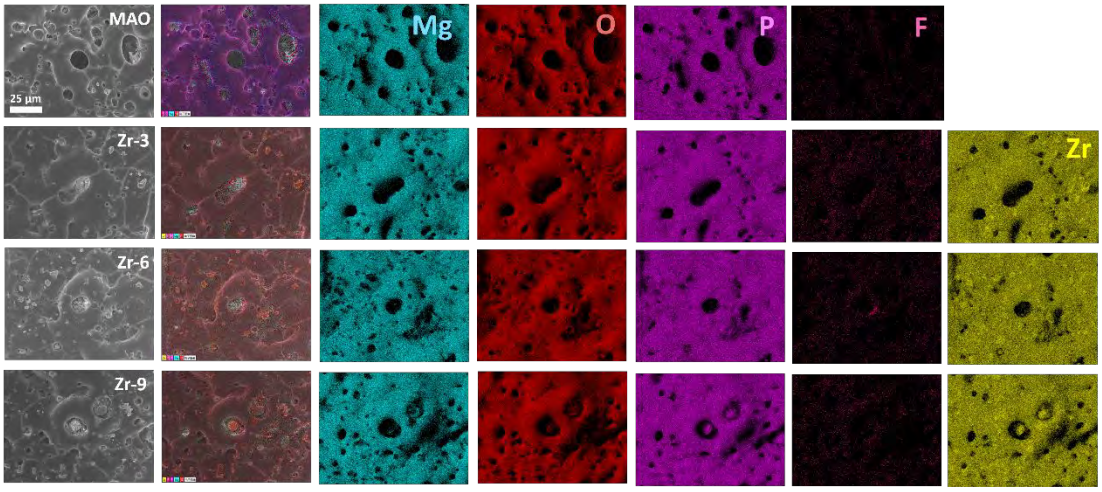


**Fig. S1.** EDS spectra of the MAO coatings doped with different concentrations of $ZrO_2$ nanoparticles on ZK61 alloy.

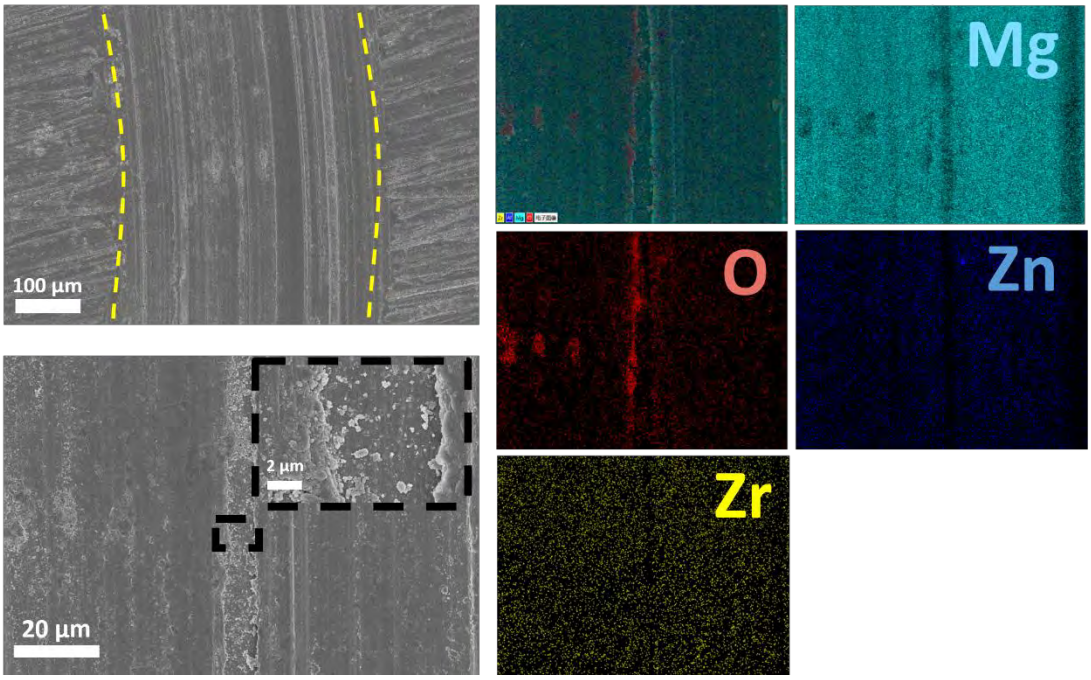


**Fig. S2.** SEM images and EDS spectra of ZK61 alloy.

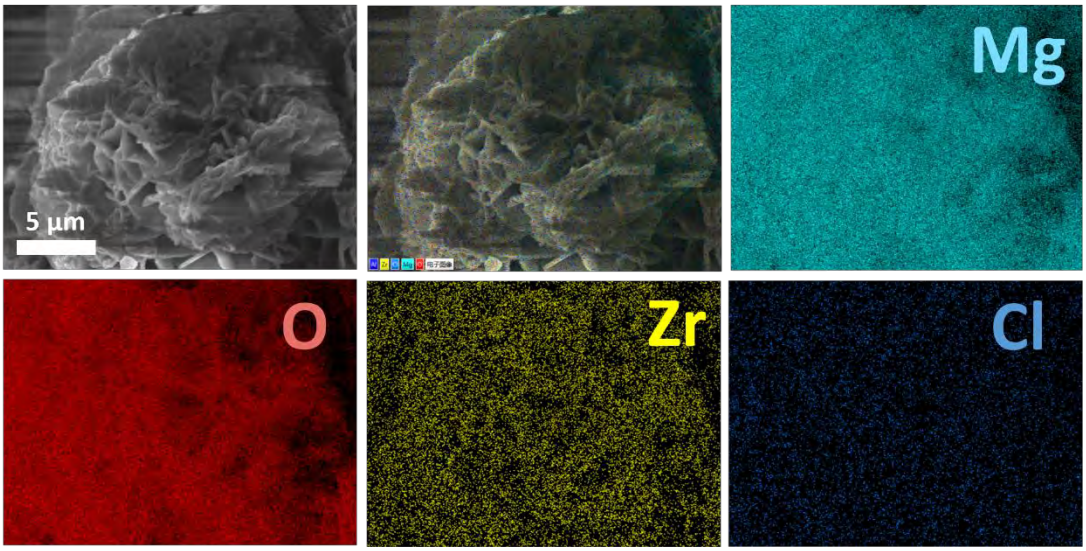


**Fig. S3.** EDS images of the ZK61 alloy immersed in the 3.5 wt% NaCl solution for 28 d.

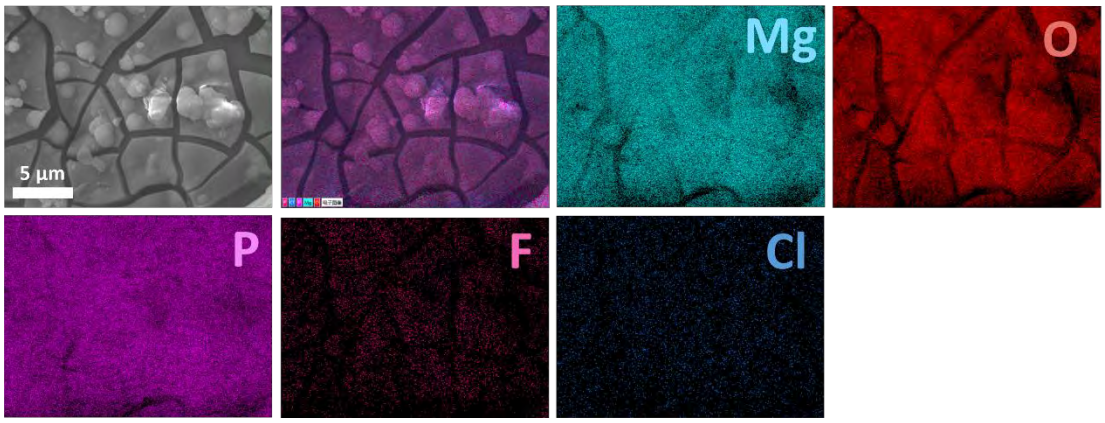


**Fig. S4.** EDS images of the MAO sample immersed in the 3.5 wt% NaCl solution for 28 d.

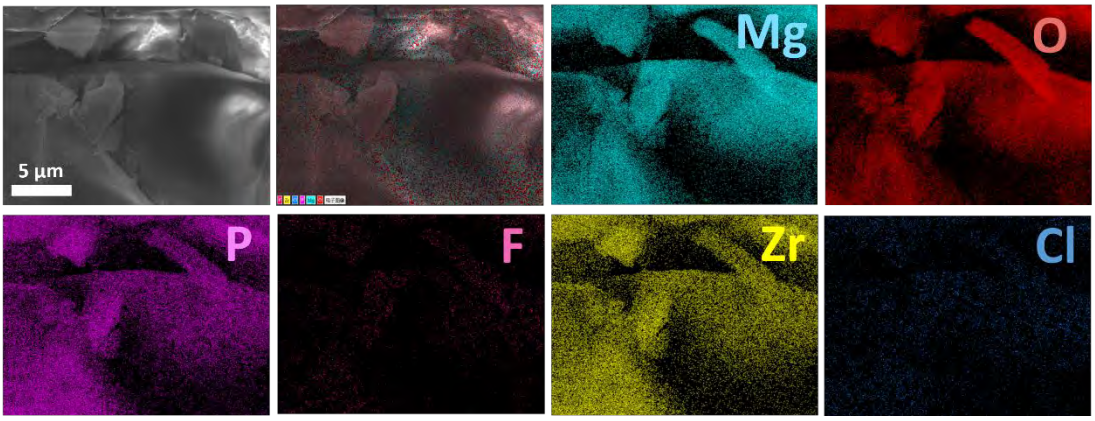


**Fig. S5.** EDS images of Zr-3 immersed in the 3.5 wt% NaCl solution for 28 d.

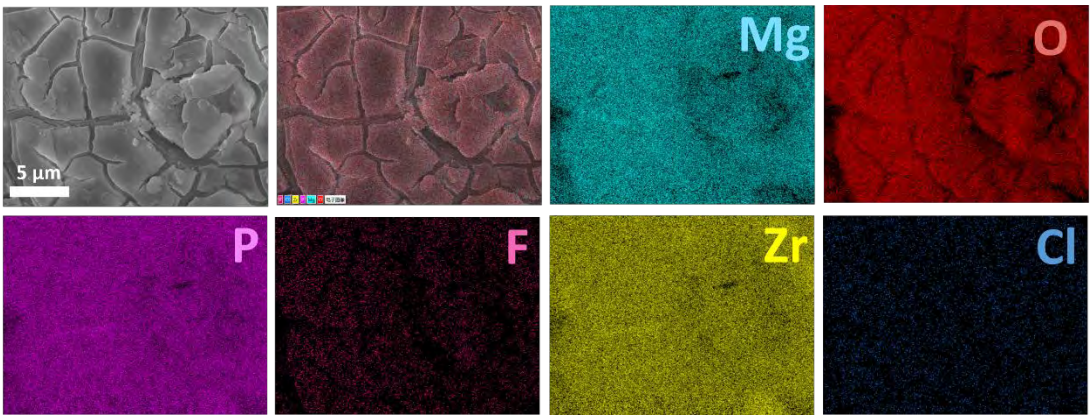


**Fig. S6.** EDS images of Zr-6 immersed in the 3.5 wt.% NaCl solution for 28 d.

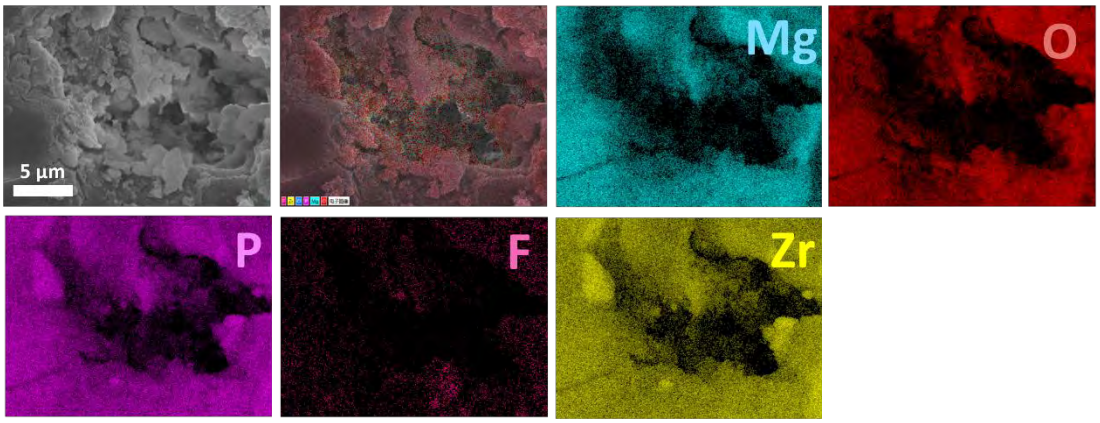


**Fig. S7.** EDS images of Zr-9 immersed in the 3.5 wt.% NaCl solution for 28 d.

**Table S1** Elemental composition (wt%) of the ZK61 alloy powder.

| Zn | Zr | Mn | Al | Fe | Ni | Cu | Si | Mg |
|---|---|---|---|---|---|---|---|---|
| 5.3085 | 0.3420 | 0.0052 | 0.0006 | 0.0045 | 0.0032 | 0.0013 | 0.0007 | 94.3340 |

**Table S2** Thickness and surface roughness ($R_a$) of MAO coatings doped with different concentrations of $ZrO_2$ nanoparticles.

| Samples | Thickness (μm) | Surface roughness ($R_a$) (μm) |
|---|---|---|
| **MAO** | 24.5±2.6 | 1.22±0.22 |
| **Zr-3** | 25.5±1.8 | 1.45±0.29 |
| **Zr-6** | 25.1±2.1 | 1.74±0.36 |
| **Zr-9** | 24.9±2.2 | 2.05±0.45 |

**Table S3** Elemental composition (at.%) of the surface of the ZK61 alloy and MAO coatings doped with different concentrations of $ZrO_2$ nanoparticles.

| | **O** | **Mg** | **P** | **Zr** | **F** |
|---|---|---|---|---|---|
| **MAO** | 61.03 | 22.16 | 15.92 | 0 | 0.88 |
| **Zr-3** | 60.8 | 19.95 | 15.83 | 2.48 | 0.94 |
| **Zr-6** | 60.4 | 19.45 | 15.19 | 3.84 | 0.91 |
| **Zr-9** | 60.27 | 18.2 | 14.51 | 5.83 | 0.89 |